論文 / 著書情報
Article / Book Information

題目(和文)	
Title(English)	Plasmonic modification of magnetic properties on metal nanostructures
著者(和文)	菊池祐介
Author(English)	Yusuke Kikuchi
出典(和文)	学位:博士(工学), 学位授与機関:東京工業大学, 報告番号:甲第11151号, 授与年月日:2019年3月26日, 学位の種別:課程博士, 審査員:田中 拓男,原 正彦,大友 明,一杉 太郎,和田 裕之,三宮 工
Citation(English)	Degree:Doctor (Engineering), Conferring organization: Tokyo Institute of Technology, Report number:甲第11151号, Conferred date:2019/3/26, Degree Type:Course doctor, Examiner:,,,,,
学位種別(和文)	博士論文
Type(English)	Doctoral Thesis

Plasmonic modification of magnetic properties on metal nanostructures

by

Yusuke Kikuchi

Submitted to the Department of Chemical Science and Engineering

for the degree of

DOCTOR OF ENGINEERING

at the

TOKYO INSTITUTE OF TECHNOLOGY

Table of Contents

Chapter 1

Introduction

Magneto-plasmonics, a new field that merges the concepts from plasmonics and magnetics, has gained increasing interest not only in the field of magnetism but also in the field of plasmonics. The typical and important topic in magneto-plasmonics is that large magneto-optical effect is observed by surface plasmon resonance. Researchers consider that this phenomenon is due to the surface plasmon excitation; it is expected that plasmon excitation can enhance the magneto-optical effect beyond its current limitation. However, at present, it is not clear whether the enhancement of the magneto-optical effect by surface plasmon excitation is genuine or not due to the lack of evidence. Therefore, it is important to clarify the relationship between magneto-optical effect enhancement and surface plasmon excitation through experiment to realize unique optical devices such as a high-resolution spatial light modulator. Moreover, magneto-plasmonics is still in its infancy and there is still much unexplored physics to be discussed especially on the interaction between surface plasmons and magnetization.

In this chapter, first, the background knowledge of plasmonics is provided. Second, a brief research history of the correlation between magnetics and optics (magneto-optics) is given. Then, a review of the current research on magneto-plasmonics is introduced. Finally, the focus point of this research is defined.

1.1 Plasmonics

Plasmonics is the study of the optical phenomena induced by and associated with surface plasmons. The first part of this section explains plasmons. Subsequent part describes the two kinds of plasmons: (1) propagating surface plasmons, and (2) localized surface plasmons.

1.1.1 Plasmons

A plasmon is a quantum of collective oscillations of free electrons in a material, arising from the quantization of plasma oscillations. This phenomenon is observed in free-electron-like metals. The dielectric constant of metal ($\varepsilon_m(\omega)$) is expressed as $\varepsilon_m(\omega) = 1 - (\frac{\omega_p}{\omega})^2$, where ω_p is the plasma frequency in metal [1.1]. The electromagnetic properties related to the electron plasma effects are significantly different from the properties of the ordinary dielectric materials in the frequency range below the plasma frequency where the real part of a dielectric constant is negative. Light below the plasma frequency is reflected because the electrons in metal screen the electric field of light. Light above the plasma frequency is transmitted because the electrons cannot respond fast enough to screen it [1.2].

Surface plasmons are the electron plasma oscillations near a metal surface and interact strongly with light. There are two types of surface plasmons: propagating surface plasmons and localized surface plasmons. Each is described in the following subsections.

1.1.2 Propagating surface plasmons

Surface plasmons polariton (SPP) propagates along the interface of a metal and a dielectric material, including a combination of electromagnetic waves and surface charge density wave [1.1]. This surface plasma wave is a TM-polarized wave whose magnetic vector is perpendicular to the direction of the propagation of the SPP and parallel to the plane of interface [1.3]. A schematic of SPP propagation is given in Fig. 1-1. Plasmons propagate along the metal-dielectric interface, and decay evanescently away from the interface. In metals, the field decay is larger than in dielectric material owing to small penetration depth. SPPs continue to propagate along the interface until the energy they have is lost due to ohmic loss or through scattering. It has been observed that SPPs cannot be directly excited by light irradiation because the SPP dispersion lies to the right of light line [1.4]. The resulting wavevector / phase mismatch prevents the direct excitation of SPP to light [1.5]. The excitation of SPPs can be performed by using either a prism (Otto and Kretchman configuration) or a diffraction grating of appropriate pitch [1.6].

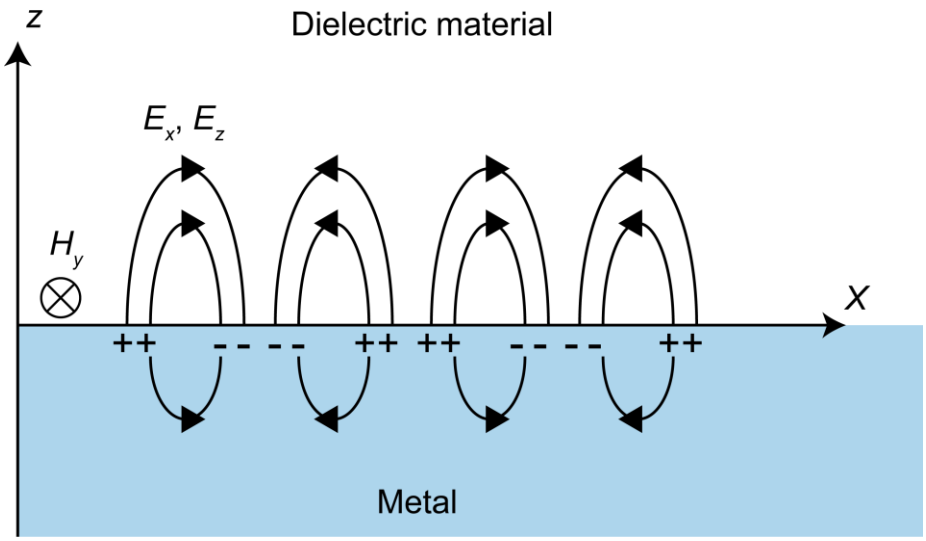

Figure 1-1. Sketch of charge oscillations and electric fields for SPP in a metal/dielectric interface. *E* and *H* are the electric field and the magnetic field, respectively.

1.1.3 Localized surface plasmons

Localized surface plasmons (LSPs) are charge density oscillations confined to a metallic nanostructure [1.7]. As shown in Fig. 1-2, when the size of a metallic nanostructure is smaller than the wavelength of incident light, the electric field of the light induces waves of collective electron oscillations confined to the surface of the nanoparticle, which is the LSP resonance [1.7]. This wave motion is composed of different orders, from the lowest dipolar to higher order multipoles, depending on the size of the nanostructure relative to the wavelength of light [1.7]. However, in the case that the nanostructure size is much smaller than the wavelength of incident light, the electron oscillation can be considered to be predominantly dipolar [1.7].

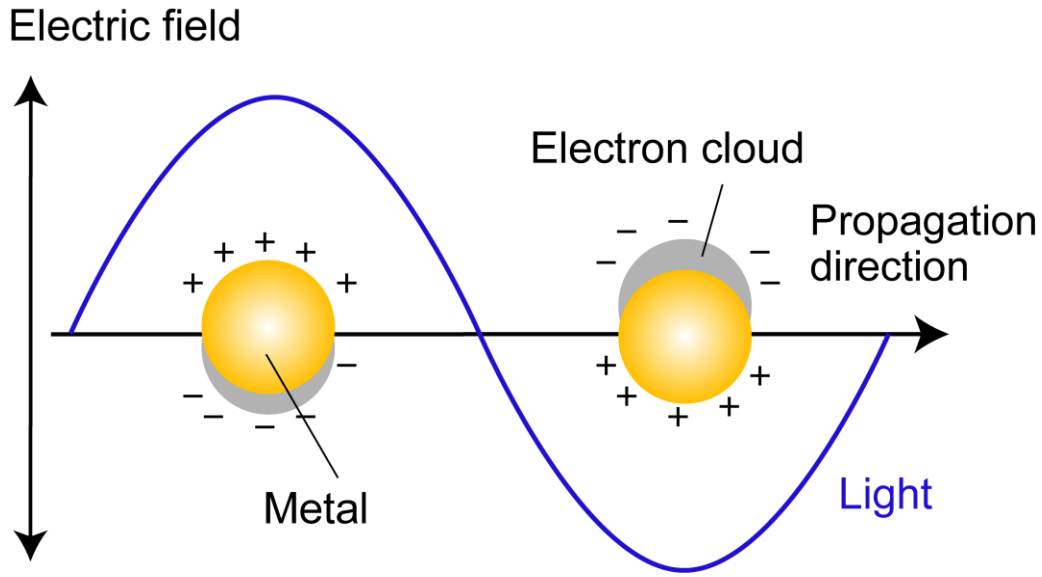

Figure 1-2. Sketch of charge oscillation for LSP in a metallic nanoparticle.

The dipolar polarizability (α_j) along one of the principal axes *j* is expressed as,

$$\alpha_j = V\varepsilon_s(\omega)\frac{\varepsilon(\omega)-\varepsilon_s(\omega)}{\varepsilon_s(\omega)+L_j(\varepsilon(\omega)-\varepsilon_s(\omega))}, \quad (1.1)$$

where V is the volume of the nanostructure, $\varepsilon_s(\omega)$ is the permittivity of the medium surrounding the nanostructure, $\varepsilon(\omega)$ is the permittivity of the nanostructure's substance, and L_j is the depolarization factor that satisfies the condition $L_x + L_y + L_z = 1$ [1.8]. The depolarized field inside the nanostructure is induced by the incident electric field and is related to L_j, which is dependent on the shape of the nanostructure [1.9]. For a spherical nanoparticle, $L_x = L_y = L_z = 1/3$. When the denominator in Eq. (1.1) is zero, $\varepsilon(\omega) = -2\varepsilon_s(\omega)$ resulting in a significant polarization induced in the nanostructure, which means that LSP resonance is excited. For an elliptical nanostructure, the values of L_x, L_y,

and L_z are different. When the length of *x*-axis is longer than the ones of *y* and *z* axis, L_x is smaller compared to L_y and L_z ($L_x < L_y$ and L_z). Since a larger value of $\varepsilon(\omega)$ is required to excite the LSP resonance associated with the *x*-axis [1.8, 1.10], a long wavelength resonance is present in the spectrum when light is polarized along the *x*-axis (long axis). This LSP is commonly named as longitudinal LSP. The resonance associated with the *y* and *z*-axis (short axis) appears at shorter wavelengths and is commonly named as transversal LSP. In the elliptical nanostructure, the resonant wavelength of both the longitudinal and transverse LSP can be tuned by changing the structure's aspect ratio.

The LSP resonance strongly depends on the material, size, geometry, dielectric environment surrounding the nanostructure, and separation distance of the nanostructures. In LSP experiments at the visible region, common material used for nanostructure fabrication are metals such as silver (Ag), copper (Cu), and gold (Au) [1.11].

When LSP is resonantly excited by light, certain optical characteristics are observed. First, strong light absorption occurs at the plasmon resonant wavelength [1.12], as shown in Fig. 1-3 (a). This phenomenon has already been used in stained glass. Second, an intense electric field on the surface of the nanostructure is generated by the electron oscillation induced by the incident electric field [1.13], as shown in Fig. 1-3 (b). The magnitude of the plasmon resonance-induced electric field decreases drastically as it moves far away from the nanostructure surface, but the attained maximum electric field is larger than the incident light [1.13]. Recently, the intense electric fields produced near plasmon resonant metallic nanoparticles are utilized in several fields, such as surface enhanced Raman spectroscopy (SERS) [1.14], catalysis activity enhancement [1.2], photovoltaic

conversion efficiency improvement [1.15], and so on.

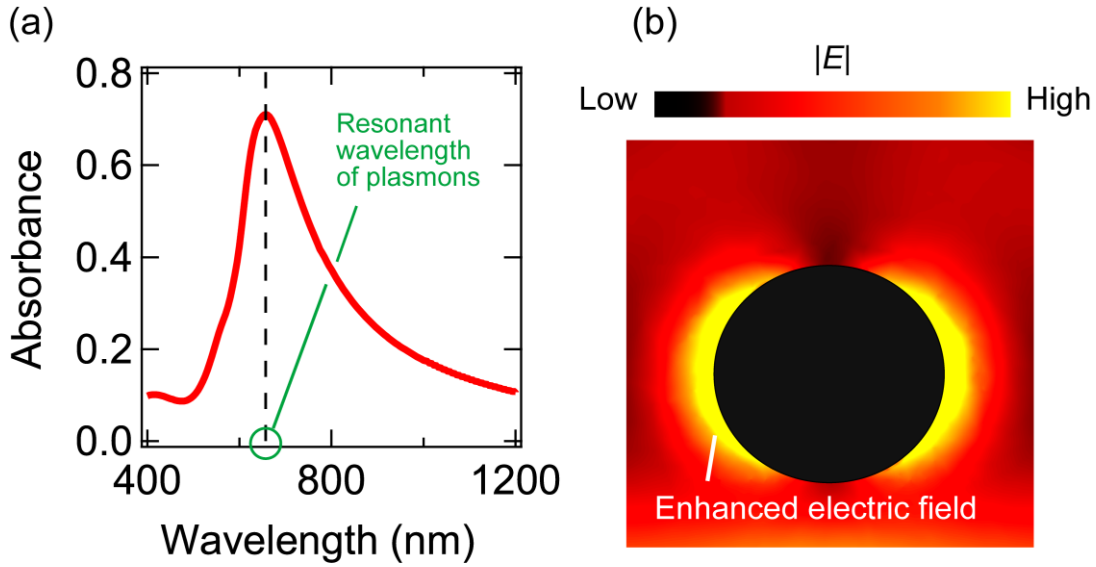

Figure 1-3. (a) Calculated absorbance spectrum of an Au nanoparticle (diameter is 100 nm). When LSPs are resonantly excited by an electromagnetic wave, a sharp absorbance peak centered at the plasmon resonance wavelength appears. (b) Calculated electric field distribution for an Au nanoparticle under LSP excitation.

1.2 Magneto-optics

In this section, the basic knowledge of magneto-optics is introduced to better understand magneto-plasmonics that will be described in the next section.

The interaction of light with materials is affected by the magnetic state of the medium, such interaction between electromagnetic radiation and magnetically polarized material results in the magneto-optical effect [1.16]. Today, two types of magneto-optical effect are widely known. The first one is the Faraday effect that describes the interaction of magnetic medium and light in a transmission geometry. Second is the magneto-optical Kerr effect (MOKE), described in the reflection geometry.

In 1845, Michael Faraday observed the first magneto-optical effect, which is now called the Faraday effect [1.17]. As shown in Fig. 1-4 (a), when polarized light passes through a transparent material such as glass along the direction of an externally applied magnetic field, the transmitted light is elliptically polarized with its major axis rotated from the incident light's initial plane of polarization [1.18]. This rotation of the plane of polarization (θ) is proportional to the propagation length of the transmitted light and the magnitude of the applied magnetic field [1.18]. Especially, in the case that the transparent material exhibits a ferromagnetic property, θ is proportional to the magnitude of the material's internal magnetization [1.19].

In 1877, Reverend John Kerr discovered the magneto-optical Kerr effect (MOKE) [1.17]. There are three different MOKE geometries, namely, polar, longitudinal, and transversal

(Fig. 1-4 (b)). These geometries are identified by the relative orientation of the plane of incident light and the magnetization in the sample. In polar geometry (polar Kerr effect), the magnetization is aligned perpendicular to the sample plane and therefore always lies in the plane of incidence. In the longitudinal geometry (longitudinal Kerr effect), the magnetization lies along the sample plane and its direction is parallel to the plane of incidence. In the transverse geometry (transverse Kerr effect), the magnetization direction also lies along the sample plane but is perpendicular to the plane of incidence. In both polar and longitudinal Kerr effects, elliptically polarized light is reflected to the sample and the polarization plane is rotated with respect to the amplitude of magnetization and its direction [1.20], which is similar to the Faraday effect. On the other hand, in the transverse Kerr effect, a change in polarization state of the reflected light is not observed but a change in the reflected intensity of the *p*-polarized light is detected [1.20].

In magnetics, the magneto-optical effect is widely used for the detection and characterization of magnetic material. Its popularity is mainly based on two factors: (1) the measurement technique is non-destructive for low laser powers since the heating is not significant; and (2) the technique allows for high time-resolutions. Moreover, the magneto-optical effect is connected to the spin-orbit coupling in magnetic material [1.17], and can also be utilized to evaluate electron spin direction and polarization in the spintronics field [1.21].

The optical characteristic of the magneto-optical effect is the polarization state of the electromagnetic wave can be easily manipulated by the usage of the magnetic material. Now magneto-optical effects are used to develop optical devices. The prominent

applications of the magneto-optical effect are isolator [1.22], and spatial light modulator [1.23, 1.24]. Recently, magneto-optical effect based micron or nanometer-scaled optical devices are actively being developed to realize holographic 3D movies [1.25, 1.26]. However, technical problems still need to be addressed. The most crucial issue is the rotation of the polarization plane induced by the magneto-optical effect is small compared to the practical amount that magneto-optical devices need. Therefore, now magneto-optical research work has focused on the development of materials with large magneto-optical activity to improve the performance of magneto-optical devices.

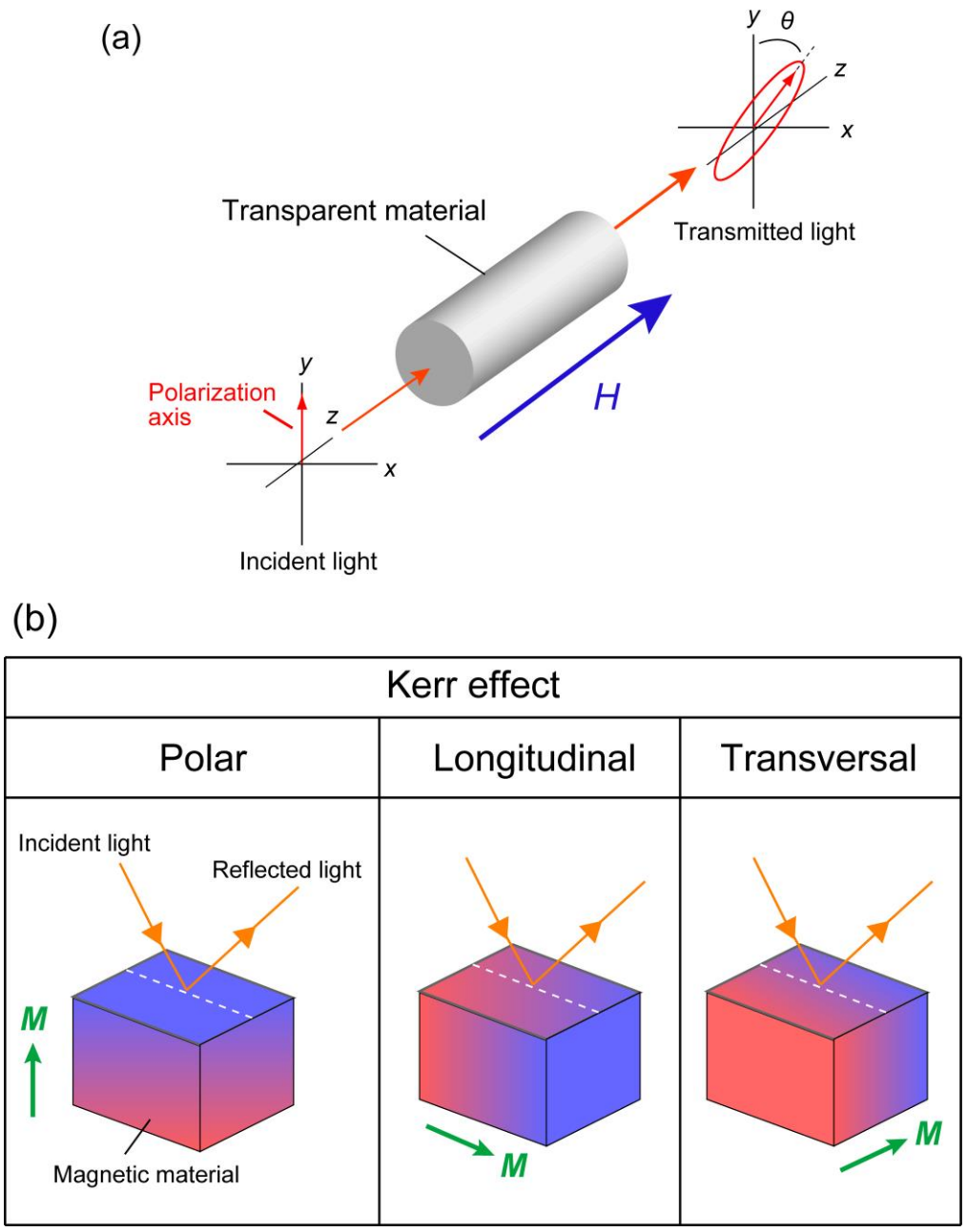

Figure 1-4. Magneto-optical effect for (a) transmission (Faraday effect) where H and θ are the applied magnetic field and polarization rotation angle, respectively. (b) Magneto-optical effect for reflection (Kerr effect). The three configurations, defined by the relative orientation between the magnetization direction ($\boldsymbol{M}$) of the magnetic material and the plane of incidence, are illustrated.

1.3 Magneto-plasmonics

Magneto-plasmonics, a research field that merges concepts from plasmonics and magnetism, has rapidly developed over the years [1.27, 1.28]. Magneto-plasmonics offers the unique possibility to manipulate light by the use of magnetic materials. The typical and important topic in magneto-plasmonics is the enhancement of the magneto-optical effect by surface plasmon resonance. In the last decade, some research groups have reported that a large magneto-optical effect is observable at the resonant wavelength of surface plasmons [1.29 – 1.33]. For a magneto-optical effect based photonic device, the excitation of surface plasmon resonance is one possible performance enhancement tool of the magneto-optical effect in the device.

As described in **section 1.1.3**, when surface plasmon resonance is excited, a localized high intensity electromagnetic field is created. This generated electric field is applied for to improve functionality such as in catalysis [1.2], and solar cells [1.15]. This enhancement phenomenon is called the field enhancement effect. However, the magneto-optical effect is intrinsically independent to light intensity [1.34]. The mechanism behind the magneto-optical enhancement by plasmon resonance may be different from merely the field-enhancement effect. In the current state of plasmonic enhancement of the magneto-optical effect, a theoretically plausible explanation as to why the large magneto-optical effect occurs at the plasmon resonance excitation wavelength has not been presented and the enhancement mechanism is not fully understood. Moreover, in order to provide evidence of surface plasmon resonance-induced enhancement of magneto-optical activity, researchers show that the peak wavelength in the magneto-optical effect spectrum is consistent with the peak wavelength in the transmittance (or reflection)

spectrum of the sample [1.29 – 1.33]. It is insufficient to assert the relationship between surface plasmon excitation and the magneto-optical effect enhancement because originally the magneto-optical effect shows wavelength dependence [1.35]. Therefore, it is not clear whether the magneto-optical effect enhancement by surface plasmon excitation is genuine or not.

Now, research in magneto-plasmonics focuses not only on the plasmonic enhancement of magneto-optical effect but also in various topics such as the magnetic field modulation of the surface plasmons wave vector [1.36, 1.37], and spin current generation by the surface plasmon resonance [1.38]. However, the mechanism of plasmonic modulation of the magnetization in magnetic material is yet to be realized and the interaction between surface plasmons and magnetization contains unexplored physics and is still in its infancy.

1.4 The scope of this research

The focal interest and motivation of this thesis is the clarification of the interaction between the magnetic property and the surface plasmons excitation. This thesis consists of two projects that focus on the different properties. The first is the magneto-optical Kerr effect enhancement by surface plasmon excitation, and the second is the magnetic anisotropy energy modulation by surface plasmon excitation.

1.4.1 The remaining Chapters of this thesis

In **Chapter 2**, the theoretical framework of the magneto-optical effect from a macroscopic view is introduced. The basic principle and experimental setup of the magneto-optical Kerr effect measurement are also presented. Then, theoretical and experimental work on polarization dependence of longitudinal magneto-optical Kerr effect in cobalt (Co) thin film and Co nanostructure was carried out. This is an essential issue to determine the sample structure used in **Chapter 3**. It is shown that the shape induced longitudinal magneto-optical Kerr effect can be ignored in a rectangular shaped Co nanostructure.

Chapter 3 presents the experimental results of the longitudinal magneto-optical Kerr effect measurements while changing the polarization direction of incident light. The LSP excitation state can be switched on or off by changing the polarization direction of the incident light in the Au/Co/Au rectangular-shaped nanostructure described in this chapter. Using this device, a clear enhancement of the longitudinal magneto-optical effect is

observed by the LSP excitation. The enhancement of the magneto-optical figure of merit in the magneto-plasmonic nanostructure by LSP excitation is also discussed.

Chapter 4 provides the experimental results of magnetic anisotropy energy modulation by LSPs. The magnetization loops obtained from the magnetic field dependence of the polar magneto-optical Kerr effect shows significant change when the LSPs are excited. From these loops, in-plane magnetic anisotropy energy increase by the plasmon resonance is estimated. The mechanism of in-plane magnetic anisotropy enhancement by the plasmon resonance is also discussed.

Finally, **Chapter 5** gives the summary and conclusions.

1.5 References

1.1. A. V. Zayats, and I. I. Smolyaninov, JOURNAL OF OPTICS A: PURE AND APPLIED OPTICS **5**, S16 (2003).

1.2. W. Hou, and S. B. Cronin, Advanced Functional Materials **23**, 1612 (2013).

1.3. J. Homola, S. S. Yee, and G. Gauglitz, Sensors and Actuators **B54**, 3 (1999).

1.4. S. Kawata, Y. Inouye, and P Verma, Nature Photonics **3**, 388 (2009).

1.5. N. Matthaiakakis, H. Mizuta, and M. D. B. Charlton, Scientific reports **6**, 1 (2016).

1.6. F. H'Dhili, T. Okamoto, J. Simonen, and S. Kawata, Optics Communications **284**, 561 (2011).

1.7. P. K. Jain, M. A. El-Sayed, Chemical Physics Letters **487**, 153 (2010).

1.8. V. Myroshnychenko, J. Rodrı´guez-Ferna´ndez, I. Pastoriza-Santos, A. M. Funston, C. Novo, P. Mulvaney, L. M. Liz-Marza´n, and F. J. Garcı´a de Abajo, Chemical Society Reviews **37**, 1792 (2008).

1.9. L. A. Golovan', P. K. Kashkarov, and V. Y. Timoshenko, Physical Properties of Crystals **52**, 697 (2007).

1.10. B. T. K. Sau, A. L. Rogach, F. Ja¨ckel, T. A. Klar, and J. Feldmann, Advanced Materials **22**, 1805 (2010).

1.11. L. M. Liz-Marza´n, Langmuir **22**, 32 (2006).

1.12. K. M. Mayer, and J. H. Hafner, Chemical Reviews **111**, 3828 (2011).

1.13. R. Yu, L. M. Liz-Marzan, and F. J. G. Abajo, Royal society of Chemistry **46**, 6710 (2017).

1.14. P. Dawson, J. A. Duenas, M. G. Boyle, M. D. Doherty, S. E. J. Bell, A. M. Kern,

O. J. F. Martin, A. S. Teh, K. B. K. Teo, and W. I. Milne, Nano Lett. **11**, 365 (2011).

1.15. H. H. Shen, P. Bienstman, and B. Maes, J. Appl. Phys. **106**, 073109 (2009).

1.16. T. Haider, International Journal of Electromagnetics and Applications **7**, 17 (2017).

1.17. Z. Q. Qiu, and S. D. Bader, REVIEW OF SCIENTIFIC INSTRUMENTS **71**, 1243 (2000).

1.18. H. S. Bennett, and E. A. Stern, Physical Review **18**, A448 (1965).

1.19. J. T. Ho, and J. D. Litster, Physical Review B **2**, 4523 (1970).

1.20. G. Armelles, Al. Cebollada, A. García-Martín, and M. U. González, Advanced Optical Materials **1**, 10 (2013).

1.21. X. Lou, C. Adelmann, S. A. Crooker, E. S. Garlid, J. Zhang, K. S. Madhukar, S. D. Flexner, C. J. Palmstrom, and P. A. Crowell, Nature Physics **3**, 197 (2007).

1.22. W. Van Parys, B. Moeyersoon, D. Van Thourhout, R. Baets, M. Vanwolleghem, B. Dagens, J. Decobert, O. Le Gouezigou, D. Make, R. Vanheertum, and L. Lagae, Applied Physics Letter **88,** 071115 (2006).

1.23. J. Park, J. Y. Cho, K. Nishimura, and M. Inoue, Japanese Journal of Applied Physics **41**, 1813 (2002).

1.24. K. Aoshima, K. Machida, D. Kato, T. Mishina, K. Wada, Y. F. Cai, H. Kinjo, K. Kuga, H. Kikuchi, T. Ishibashi, and N. Shimidzu, Journal of Display Technology **11**, 129 (2015).

1.25. N. Funabashi, K. Aoshima, K. Machida, K. Kuga, T. Ishibashi, and N. Shimidzu, IEEE Transactions on Magnetics **46**, 1998 (2010).

1.26. K. Aoshima, N. Funabashi, K. Machida, Y. Miyamoto, K. Kuga, T. Ishibashi,

N. Shimidzu, and F. Sato, Journal of Display Technology **6**, 374 (2010).

1.27. G. Armelles, A. Cebollada, A. Garcia-Martin, and M. U. Gonzalez, Advanced Optical Materials **1**, 10 (2013).

1.28. D. Sander, S. O. Valenzuela, D. Makarov, C. H. Marrows, E. E. Fullerton, P. Fischer, J. McCord, P. Vavassori, S. Mangin, P. Pirro, B. Hillebrands, A. D. Kent, T. Jungwirth, O. Gutfleisch, C. G. Kim, and A. Berger, Journal of Physics D-Applied Physics **50**, 363001 (2017).

1.29. D. Meneses-Rodriguez, E. Ferreiro-Vila, P. Prieto, J. Anguita, M. U. Gonzalez, J. M. Garcia-Martin, A. Cebollada, A. Garcia-Martin, and G. Armelles, Small **7**, 3317 (2011).

1.30. N. Maccaferri, A. Berger, S. Bonetti, V. Bonanni, M. Kataja, Q. H. Qin, S. van Dijken, Z. Pirzadeh, A. Dmitriev, J. Nogues, J. Akerman, and P. Vavassori, Physical Review Letters **111**, 167401 (2013).

1.31. H. Yamane, K. Takeda, and M. Kobayashi, Applied Physics Letters **106**, 052409 (2015).

1.32. C. A. Herreño-Fierro, E. J. Patiño, G. Armelles, and A. Cebollada, Applied Physics Letters **108**, 021109 (2016).

1.33. B. C. Choi, H. Xu, G. Hajisalem, and R. Gordon, Applied Physics Letters **112**, 022403 (2018).

1.34. D. Budker, W. Gawlik, D. F. Kimball, S. M. Rochester, V. V. Yashchuk, and A. Weis, Reviews of Modern Physics **74**, 1153 (2002).

1.35. K. Sato, H. Hongu, H. Ikekame, Y. Tosaka, M. Watanabe, K. Takanashi and H. Fujimori, Japanese Journal of Applied Physics **32**, 989 (1993).

1.36. D. Martín-Becerra, J. B. González-Díaz, V. V. Temnov, A. Cebollada, G.

Armelles, T. Thomay, A. Leitenstorfer, R. Bratschitsch, A. García-Martín, and M. González, Applied Physics Letters **97**, 183114 (2010).

1.37. V. V. Temnov1, G. Armelles, U. Woggon, D. Guzatov, A. Cebollada, A. Garcia-Martin, J. Garcia-Martin, T. Thomay, A. Leitenstorfer, and R. Bratschitsch, Nature Photonics **4**, 107 (2010).

1.38. K. Uchida, H. Adachi, D. Kikuchi, S. Ito, Z. Qiu, S. Maekawa, and E. Saitoh, Nature Communications **6**, 1 (2015).

Chapter 2

Construction of the longitudinal magneto-optical Kerr effect measurement system

The evaluation of magnetic property for this work were done using magneto-optical Kerr effect (MOKE) measurement system. In this chapter, first, the theory for magneto-optical effect (MO effect) is explained. Second, the measurement principle and experimental setup for evaluating the longitudinal magneto-optical Kerr effect (L-MOKE) is introduced. Finally, by using my L-MOKE measurement system, the L-MOKE of the *s*-wave and *p*-wave in Co thin film and Co rectangular nanostructure were experimentally evaluated.

2.1 The origin of magneto-optics

The MO effect is the study of the reflection or transmission of polarized light by a substance that is subjected to a magnetic field. This reflection or transmission can produce several effects, including (1) rotation of polarization direction (θ) of the linearly polarized incident light, and (2) introduction of ellipticity (η) to the reflected beam. The η represents the ratio of the long axis and the short axis in elliptically polarized light. From an optics view point, θ is equal to the phase difference between the right circular polarization (RCP) and left circular polarization (LCP) in the reflected or transmitted light. The η comes from the difference of absorption of RCP and LCP in material.

Macroscopically, the MO response can be expressed by the permittivity in the material [2.1]. In an isotropic material without magnetization (*M*), the dielectric tensor ($\tilde{\varepsilon}$) is described as [2.1],

$$\tilde{\varepsilon} = \begin{pmatrix} \varepsilon_{xx} & 0 & 0 \\ 0 & \varepsilon_{xx} & 0 \\ 0 & 0 & \varepsilon_{xx} \end{pmatrix}, \tag{2.1}$$

where ε_{xx} is the diagonal matrix element. For isotropic material, the diagonal elements are identical and the off-diagonal elements are zero. The presence of *M* establishes a symmetry break of permittivity and induces a uniaxial anisotropy of permittivity, resulting in off-diagonal elements. The dielectric tensor in the isotropic material with *M* is described as [2.1],

$$\tilde{\varepsilon} = \varepsilon_{xx} \begin{pmatrix} 1 & -iQM_z & iQM_y \\ iQM_z & 1 & -iQM_x \\ -iQM_y & iQM_x & 1 \end{pmatrix}, \tag{2.2}$$

where M_i is the direction cosines of the magnetization vector, with respect to the crystallographic axes; Q is the magneto-optical constant. Next, the effective refractive index ($\check{n}$) is related to the dielectric constant at the visible region through the following equation,

$$\check{n}^2 = \check{\varepsilon}. \tag{2.3}$$

Maxwell's equation combined with Eq. (2.2) and Eq. (2.3) yields the refractive index with respect to *M*, such a calculation results in two solutions of the refractive indices of RCR (n_{R}) and LCP (n_{L}) [2.2]:

$$n_{\mathrm{R}} = n(1 + \frac{1}{2} Q\boldsymbol{M} \cdot \boldsymbol{k}), \tag{2.4}$$

$$n_{\mathrm{L}} = n(1 - \frac{1}{2} Q\boldsymbol{M} \cdot \boldsymbol{k}), \tag{2.5}$$

where $\boldsymbol{k}$ is the unit vectors of the propagation direction of light, and $\boldsymbol{M}$ is the direction of the magnetization. In this way, a magnetic material has two different refractive indices, which is called magnetic birefringence. Generally, the refractive index is a complex number, where the real part of the refractive index gives the factor by which the phase velocity of light is decreased in a material as compared with vacuum. Comparing to Eq. (2.4) and Eq. (2.5), the different real part in the refractive index results in deviating phase velocity for RCP and LCP. Therefore, the rotation of the polarization plane occurs. The imaginary part of the refractive index characterizes the light extinction. The imaginary parts of n_{R} and n_{L} causes different absorption for RCP and LCP. Hence, linear polarized light transforms to elliptical polarized light.

2.2 Experimental setup for magneto-optical Kerr effect measurement

In this study, L-MOKE measurement system by combining the photoelastic modulator (PEM) and linear polarizer was constructed.

2.2.1 Measurement principle

In this section, the basic principle for measuring θ and η using a PEM is qualitatively introduced. PEM consists of a piezo-vibrator and a transparent crystal that, when unstressed, has an isotropic refractive index. By driving a piezo-vibrator at a certain frequency (p), a periodic strain is induced in one axis of the crystal. As a result, light birefringence is induced in the crystal. As shown in Fig. 2-1 (a), when light passes through the PEM, light receives a periodically varying phase retardation (δ), which is described by

$$\delta = \delta_0 \sin 2\pi p t, \tag{2.6}$$

where δ_0 is the amplitude of retardation and t is time [2.3]. Figure 2-1 (b) shows the time dependence of the phase retardation produced by the modulator and Figure 2-1 (c) shows the polarization state of the light passing through the PEM at a certain time [2.4]. The polarizing angle of incident light is 45° with respect to the vibrating axis of the piezo-vibrator. δ_0 is set to π/2. In this case, the maximum and the minimum of δ correspond to circularly polarized light. The variation of polarization state is linear polarization (LP) – RCP – LP – LCP – LP in one period of modulation. The magnitude of the x-component

of the electric field vector (E_x) is constant against time [2.4], as shown in Fig. 2-1 (d).

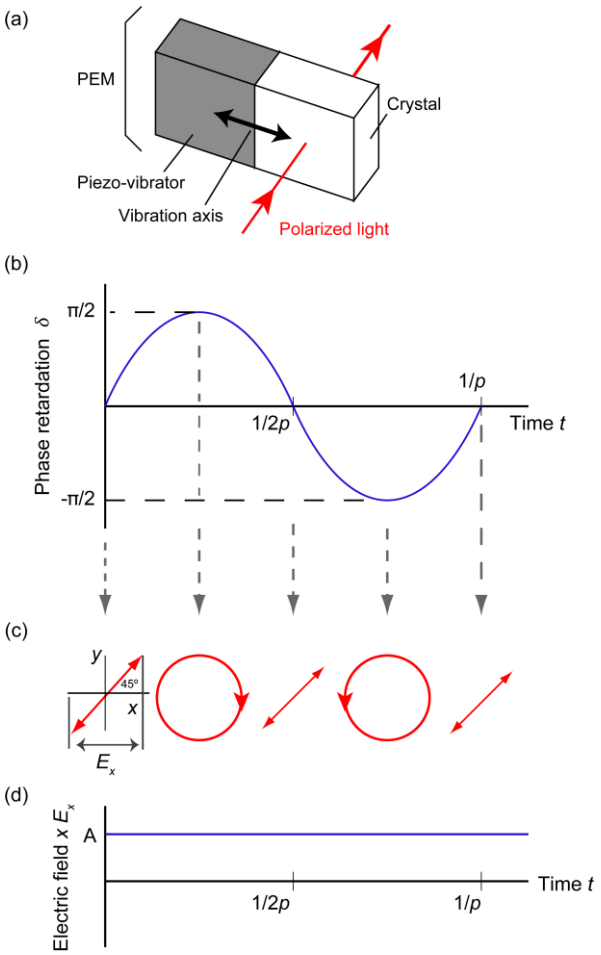

Figure 2-1. (a) Sketch of PEM. (b) The time (t) dependence of phase retardation (δ) for transmitted light passing through the PEM. p indicates the modulation frequency of the PEM. In this case, the magnitude of δ is set to $\pi/2$. (c) The polarization state of transmitted light passing through the PEM. The polarization axis of the incident linearly polarized light is set to 45 degrees with respect to the vibration axis of the PEM. (d) Time dependence of the electric field (E) corresponding to the x direction (E_x) of the transmitted light passing through the PEM.

Next, a new optical configuration when light passing through the PEM illuminates onto a sample is considered, as shown in Fig. 2-2 (a). When a difference between phase shifts for LCP and RCP such as Kerr rotation (θ_k) exists, the plane of linear polarized light is rotated, and the E_x in linear polarization is changed. Especially, if the plane is rotated along the x axis as seen in Fig. 2-2 (b), E_x is larger compared to the one without sample at $t = 0$. At the time δ equal to θ_k, E_x is same as the one without a sample as shown in Fig. 2-1 (d). Thus the $2p$ frequency component appears in the time dependence plot of E_x as shown in Fig. 2-2 (c) [2.4].

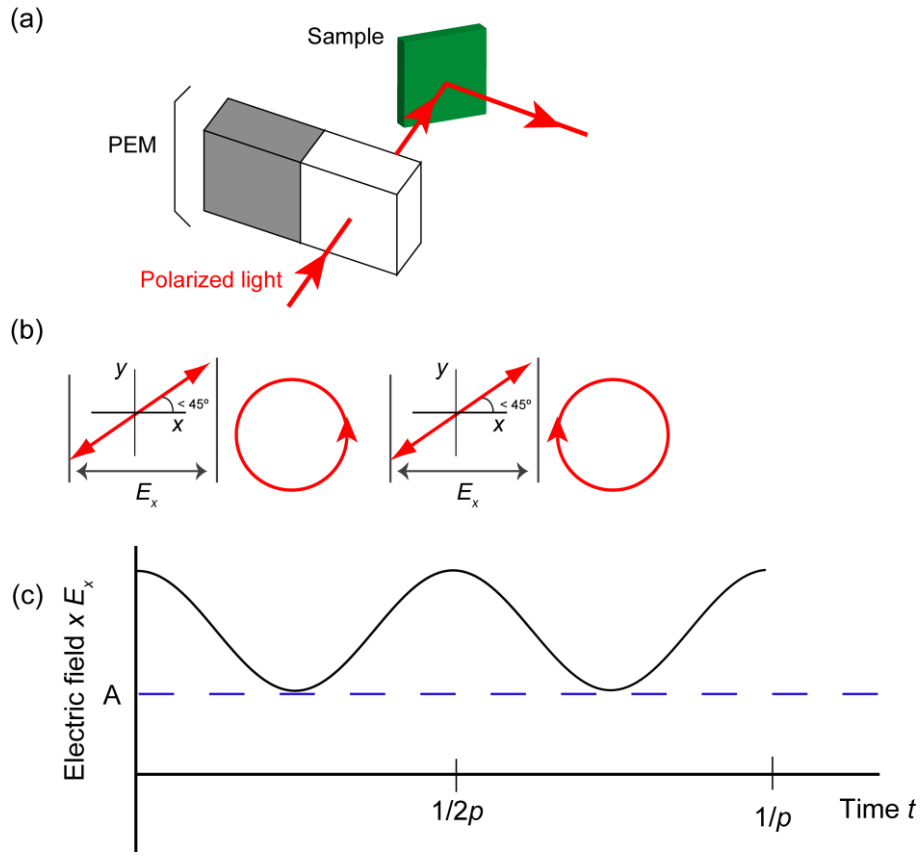

Figure 2-2. (a) The reflection configuration: linearly polarized light passes through the PEM, and then light is reflected by the sample. (b) The polarization state of the reflected light from the sample. In this case, I set an assumption that a difference between phase shifts for RCP and LCP such as Kerr rotation occurs when light is reflected by the sample. (c) Time (t) dependence of E_x in reflected light from the sample with different phase shifts in each circularly polarized light. p indicates the modulation frequency of the PEM. Blue dot line indicates the E_x without sample.

On the other hand, when an optical absorption difference between LCP and RCP like a Kerr ellipticity (η_k) is present, E_x for RCP and LCP become different as demonstrated in Fig. 2-3 (a), resulting in the appearance of a p frequency component in the time dependence plot of E_x as shown in Fig. 2-3 (b) [2.4]. In this way, signals corresponding to η_k and θ_k are obtained by detecting the p and $2p$ component of the electric field in reflected or transmitted light.

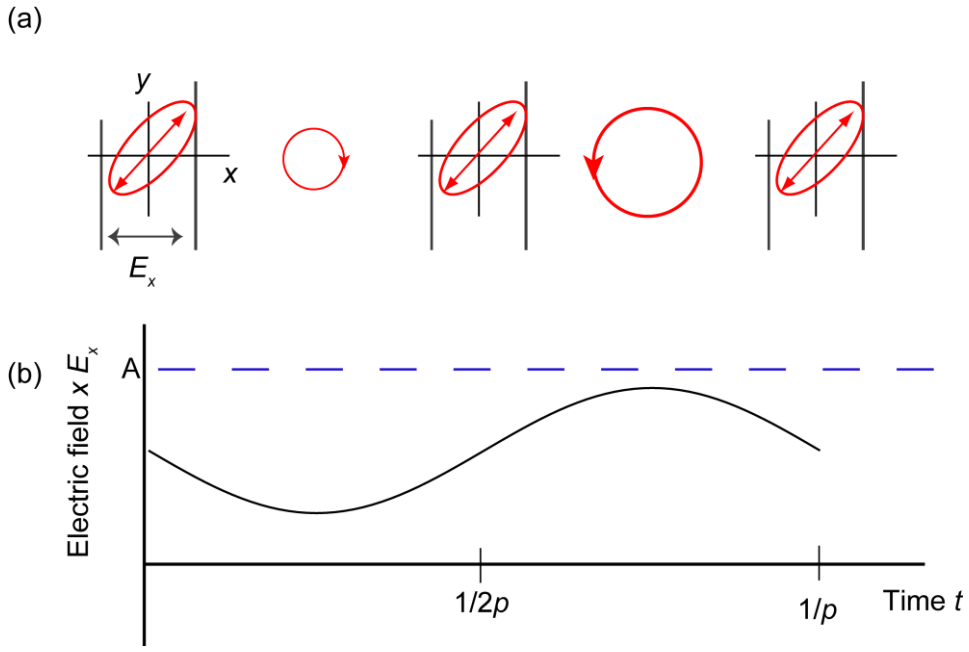

Figure 2-3. (a) The polarization state of the reflected light from the sample. In this case, I set an assumption that an optical absorption difference between RCP and LCP such as Kerr ellipticity occurs when light is reflected by the sample. (c) The time (t) dependence of E_x in reflected light from the sample with different optical absorption for each circularly polarized light. p indicates the modulation frequency of the PEM. Blue dot line indicates the E_x without sample.

2.2.2 Theoretical description of the MO signal detection

A schematic diagram showing the principle of the MOKE measurement method is given in Fig. 2-4. The coordinates are as shown in the figure; the *z* axis is parallel to the direction of propagation of incident light. The *y* axis is located in the plane of incident, while, the *x* axis is perpendicular to the *yz* plane. A polarizer is placed in the illumination path to generate linearly polarized incident light. The polarizing angle of the polarizer (P) is defined with respect to *x*-axis as φ. When φ is set to 0° or 90°, *p* or *s*-polarized light illuminates the sample. The reflected light passes through the PEM and analyzer (A). The vibrating axis of the PEM is aligned to the φ = 0 degrees of P. The polarizing axis of A makes an angle of 45° with respect to the φ = 0 degrees of P. The amplitude of the electric field of reflected light E_φ pass through A is described below [2.4],

$$E_\varphi = \frac{E}{2\sqrt{2}}\left\{r_+\left(1 - ie^{i\delta}\right)e^{i\varphi} + r_-\left(1 + ie^{i\delta}\right)e^{-i\varphi}\right\}, \tag{2.7}$$

where *E* is the amplitude of electric field of the incident polarized light; δ is the phase retardation given by the PEM operation: $r_\pm$ are the Fresnel coefficients of the sample; $r_+ = |r_+|\exp(i\theta_+)$ and $r_- = |r_-|\exp(i\theta_-)$ for RCP and LCP, respectively. The light intensity detected by detector (D) (I_φ), which is proportional to $|E|^2$, is described by [2.4],

$$I_\varphi \approx \frac{E^2}{2}\left\{R + \frac{\Delta R}{2}\sin\delta + R\sin(\Delta\theta + 2\varphi)\cos\delta\right\}. \tag{2.8}$$

R, ΔR, and $\Delta\theta$ are defined as

$$R = \frac{1}{2}(|r_+|^2 + |r_-|^2), \tag{2.9}$$

$$\Delta R = |r_+|^2 - |r_-|^2, \tag{2.10}$$

$$\Delta\theta = \theta_+ - \theta_-. \tag{2.11}$$

The magneto-optical parameter, Kerr rotation θ_k and Kerr ellipticity η_k, can be expressed by using Eq. (2.9) – (2.11) in the following equations [2.4],

$$\theta_k = -\frac{\Delta\theta}{2}, \tag{2.12}$$

$$\eta_k = \frac{1}{4}\frac{\Delta R}{R}, \tag{2.13}$$

By applying Eq. (2.12) and (2.13) to Eq. (2.8),

$$I_\varphi \approx \frac{E^2}{2}R\{1 + 2\eta_k \sin\delta + \sin(2\varphi - 2\theta_k)\cos\delta\}. \tag{2.14}$$

By applying Eq. (2.6) to Eq. (2.14) and using the expansion formulae below [2.4],

$$\sin(\delta_0 \sin 2\pi pt) = 2J_1(\delta_0)\sin 2\pi pt + \cdots,$$
$$\cos(\delta_0 \sin 2\pi pt) = J_0(\delta_0) + 2J_2(\delta_0)\sin 4\pi pt + \cdots, \tag{2.15}$$

where $J_n(x)$ is an *n*-th order Bessel function, Eq. (2.14) is developed,

$$\mathrm{I} \approx I(0) + I(p)\sin 2\pi pt + I(2p)\sin 4\pi pt + \cdots, \tag{2.16}$$

in which

$$I(0) \approx A\{1 + J_0(\delta_0)\sin(2\varphi - 2\theta_k)\}, \tag{2.17}$$

$$I(p) \approx A\{2\eta_k \cdot 2J_1(\delta_0)\}, \tag{2.18}$$

$$I(2p) \approx A\{2J_2(\delta_0)\sin(2\varphi - 2\theta_k)\}, \tag{2.19}$$

where $A = \frac{{E_0}^2 R}{2}$ is defined to simplify the formula. The ratios $I(p)$ / $I(0)$ and $I(2p)$ / $I(0)$ are provided below,

$$\frac{I(p)}{I(0)} = B\,\frac{4\eta_k J_1(\delta_0)}{1+J_0(\delta_0)\sin(2\varphi-2\theta_k)}, \tag{2.20}$$

$$\frac{I(2p)}{I(0)} = C\,\frac{2J_2(\delta_0)\sin(2\varphi-2\theta_k)}{1+J_0(\delta_0)\sin(2\varphi-2\theta_k)}, \tag{2.21}$$

where *B* and *C* are the appropriate constant parameter representing the ratio of gains of the detector – amplifier system for *p* Hz and 2*p* Hz component to the DC components. For a certain value of δ_0 = 2.408 radians, J_0 = 0 [2.5], which value is obtained by calculating the Bessel function in reference. Therefore $I(p)$ / $I(0)$ is proportional to η_k,

$I(2p)$ / $I(0)$ can be expressed as a function of θ_k. Eq. (2.20) and Eq. (2.21) are given in the case of φ = 0 degrees as

$$\eta_k = \frac{1}{4BJ_1}\frac{I(p)}{I(0)}, \tag{2.22}$$

$$\theta_k = \frac{1}{2}\sin^{-1}\left(\frac{-1}{2CJ_2}\frac{I(2p)}{I(0)}\right). \tag{2.23}$$

Therefore, η_k and θ_k can be calculated from the experimental value of the DC, p and $2p$ component of light intensity that is detected by the photodetector. It is noted that in the case of φ = 90 degrees, the sign of θ_k is opposite to the one of φ = 0 degrees, while η_k has the same sign.

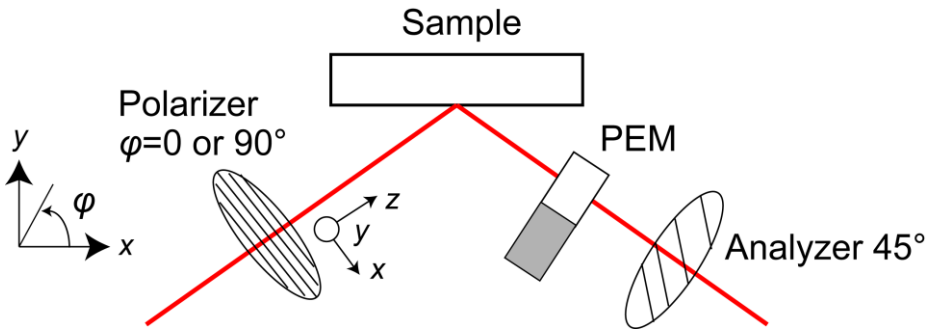

Figure 2-4. A schematic diagram of the MOKE measurement method using PEM.

Finally, the calibration method about constant values BJ_1 and CJ_2 is introduced [2.4]. For the case of CJ_2, as shown in Fig. 2-5 (a), the polarizing axis φ of polarizer is set at -

45° with respect to the *x*-axis, and also the polarizing axis of analyzer at 45°. The PEM, in which modulation axis is oriented to *x*-axis, is placed between the polarizer and analyzer. In this condition, θ_k and η_k are equal to zero because the sample is not placed in the illumination path. When the $J_0 = 0$ (δ_0 = 2.408 rad.) is set in Eq. (2.21), the value of CJ_2 is obtained as,

$$\frac{I(2p)}{I(0)} = -2CJ_2. \tag{2.24}$$

Second, when the value of BJ_1 is estimated, a quarter wave plate should be set between the PEM and the analyzer as shown in Fig. 2-5 (b). Phase retardation δ given by the PEM and the quarter wave plate is described by

$$\delta = \frac{\pi}{2} + \delta_0 \sin 2\pi pt. \tag{2.25}$$

Using φ = -45°, $\theta_k = \eta_k = 0$, and substituting Eq. (2.25) into Eq. (2.14),

$$I \approx \left\{1 - J_0 \cos\frac{\pi}{2} + 2J_1 \sin\frac{\pi}{2} \sin 2\pi pt - 2J_2 \cos\frac{\pi}{2} \sin 4\pi pt \cdots\right\}. \tag{2.26}$$

From this equation, $I(0)$ and $I(p)$ can be introduced instead of Eq.(2.17) and Eq. (2.18),

$$I(0) \approx 1 - J_0 \cos\frac{\pi}{2}, \tag{2.27}$$

$$I(p) \approx 2J_1 \sin\frac{\pi}{2}. \tag{2.28}$$

Hence,

$$\frac{I(p)}{I(0)} = 2BJ_1. \tag{2.29}$$

In this way, the coefficient value of BJ_1 is provided.

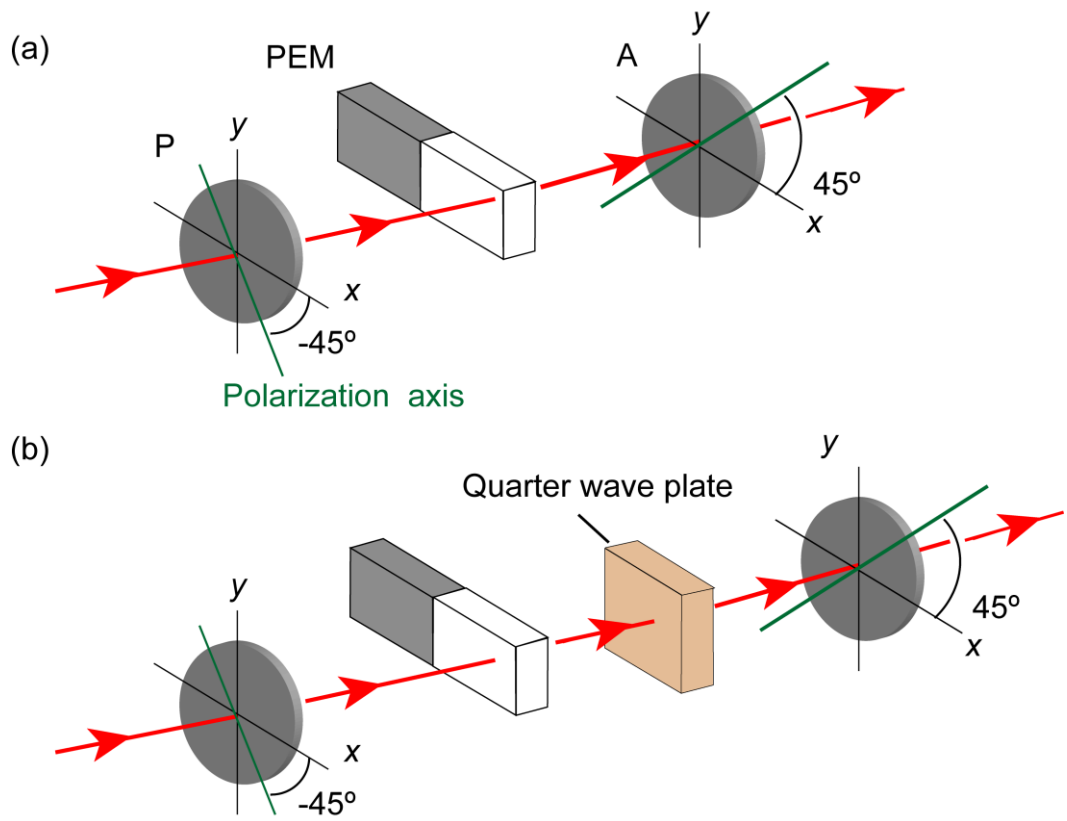

Figure 2-5. Optical configuration for calibrating constant values (a) CJ_2, and (b) BJ_1.

2.3 Determination of L-MOKE system setting

In this study, the L-MOKE with/without plasmon excitation is evaluated by changing the polarization direction of incident light (*s* or *p*), which is discussed in more detail in **Chapter 3**. If the L-MOKE response is essentially different for *s*-polarized light and *p*-polarized light, it cannot determine whether the difference of the L-MOKE response by changing the polarization direction is caused by plasmon excitation or is merely the polarization dependence of L-MOKE. So, in this section, the polarization dependence of L-MOKE response is theoretically examined based on the simplified analytic expression for MOKE of *p* and *s*-waves with different incident angle. Then, the optical layout of constructed L-MOKE measurement system is introduced.

2.3.1 Incident angle dependence of L-MOKE for *s* and *p*-polarized light

Chun-Yeol You, et al. explained that the L-MOKE response of *p* and *s*-polarized light as a function of incident angle θ_0 in the situation when light is incident from a nonmagnetic medium, 0, to a magnetic medium, 1 [2.6]. The formulae are described below,

$$\Phi_p = \frac{\cos\theta_0 \tan\theta_1}{\cos(\theta_0+\theta_1)} \cdot \frac{in_0 n_1 Q}{({n_1}^2-{n_0}^2)}, \tag{2.30}$$

$$\Phi_s = -\frac{\cos\theta_0 \tan\theta_1}{\cos(\theta_0-\theta_1)} \cdot \frac{in_0 n_1 Q}{({n_1}^2-{n_0}^2)}, \tag{2.31}$$

where Φ_p and Φ_s represent the complex Kerr rotation of *p* and *s*-polarized light,

respectively. n_0 and n_1 are the refractive indices of the nonmagnetic medium and magnetic medium, respectively. θ_1 is the complex refractive angle and Q the magneto-optical constant. By dividing Eq. (2.31) to (2.30),

$$\frac{\Phi_s}{\Phi_p} = -\frac{\cos(\theta_0+\theta_1)}{\cos(\theta_0-\theta_1)}. \tag{2.32}$$

Since the refractive angle is related to the incident angle via Snell's law,

$$n_0 \sin\theta_0 = n_1 \sin\theta_1, \tag{2.33}$$

the $\frac{\Phi_s}{\Phi_p}$ as a function of θ_0 can be estimated if material data for n_0 and n_1 at a certain wavelength is prepared. When linearly polarized light with λ = 756 nm, which is very close to the wavelength of laser used in L-MOKE system, illuminates Co (n = 2.4 + 4.64i, [2.7]) from air (n = 1), the incident angle dependence of $|\Phi_s|$ / $|\Phi_p|$ in Co shows that $|\Phi_s|$ / $|\Phi_p|$ gradually decreases with increasing θ_0 (Fig. 2-6). The minimum value of $|\Phi_s|$ / $|\Phi_p|$ occurs at θ_0 = 81°. In this study, the incident angle was set to minimum of 14° due to the clearance between optical components in the L-MOKE system. $|\Phi_s|$ / $|\Phi_p|$ at θ_0 = 14° was calculated to be 0.99 in air/Co medium. This means that the theoretical difference of $|\Phi|$ in *p*-polarized light and *s*-polarized light is about 1 % in the Co thin film, in which plasmon resonance is not excited.

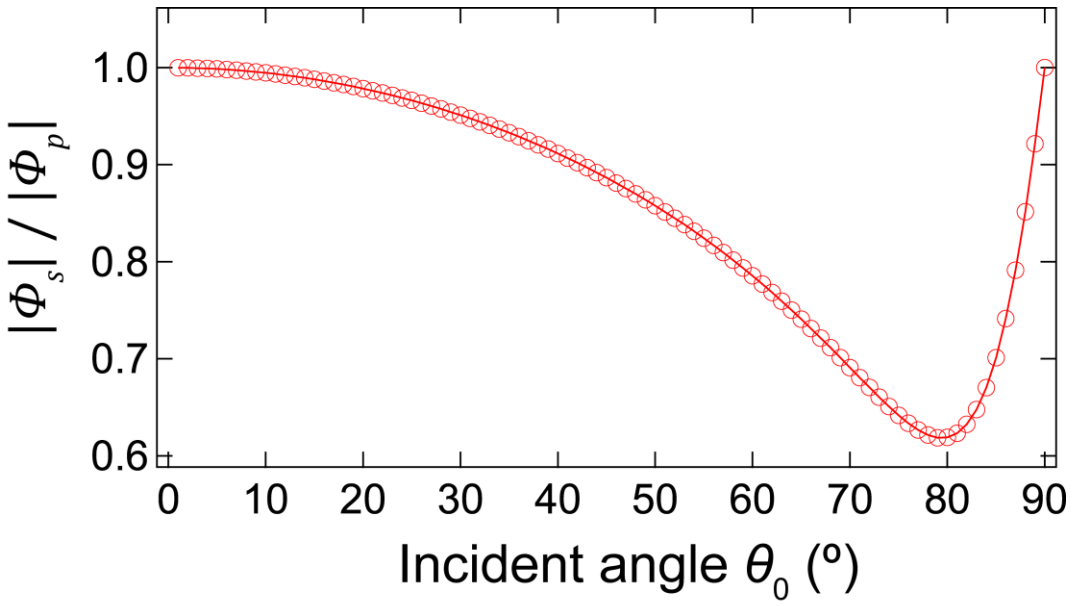

Figure 2-6. The incident angle (θ_0) dependence of the ratio of magnitude of complex Kerr rotation ($|\Phi|$) with respect to the *s*-wave ($|\Phi_s|$) and *p*-wave ($|\Phi_p|$) ($|\Phi_s| / |\Phi_p|$) in Co. The polarized light with λ = 756 nm is illuminated from air to Co.

2.3.2 Optical setup of L-MOKE measurement system

Figure 2-7 shows a block diagram and photograph of the constructed L-MOKE measurement system. In this system, CW-diode lasers were used as a light source with a wavelength λ of 640 nm (TOPTICA Photonics, iBEAM SMART 640-5) or λ = 785 nm (Showa Optronics, D785S-100-11). An ND filter was placed between the laser and the polarizer in order to adjust the light intensity. The illumination path was controlled by an aluminum (Al) mirror. The incident angle was fixed at 14°. The illuminated light was focused on the sample surface by the lens, the spot diameter size was closed to 500 μm. Two Gran-Taylor prisms (THORLABS, GT10, extinction ratio; 100,000 : 1) were used as a polarizer and analyzer. By rotating the polarization axis of the polarizer, *p*-polarized light was realized. For the case of *s*-polarized light, it was necessary to both rotate the polarization axis of the polarizer to 90° and set a half-wave plate between the light source and polarizer. The PEM module (Hinds instruments, PEM100 II/FS42) modulates the phase velocity of light at p = 42 kHz and generates 2 reference square wave signals that are fed into the lock-in amplifier (Stanford Research Systems, MODEL SR850) which measures both 1st and 2nd harmonic of the detected signal. The reflected light was focused to the Si photodetector (New Focus, Nanosecond Photodetector Model 1621) for detection. The output voltage signal from the detector corresponds to the input light intensity and is fed to a lock-in amplifier and low-pass filter (NF corporation, E-3201A). By passing the output signal through a low-pass filter, the zero frequency component of the output signal can be obtained. Detected voltage signals were simultaneously sent to a PC via an A/D converter (National instruments, DAQ NI USB-6259), and then θ_k and η_k were calculated by using LabVIEW program.

The sample was placed between two neodymium magnets (Magfine, size; ϕ 50 mm × 50 mm) in order to apply a magnetic field to the sample. The magnetic field was aligned parallel to both the sample surface and the incoming light's plane of incidence, which provides the longitudinal Kerr effect condition. The magnetic field strength was varied by adjusting the distance between the two magnets. The polarity of the magnetic field was reversed by rotating the magnets 180°. A Gauss meter was used to measure the strength and polarity of the magnetic field. The maximum magnetic field strength was estimated to be 1200 Gauss.

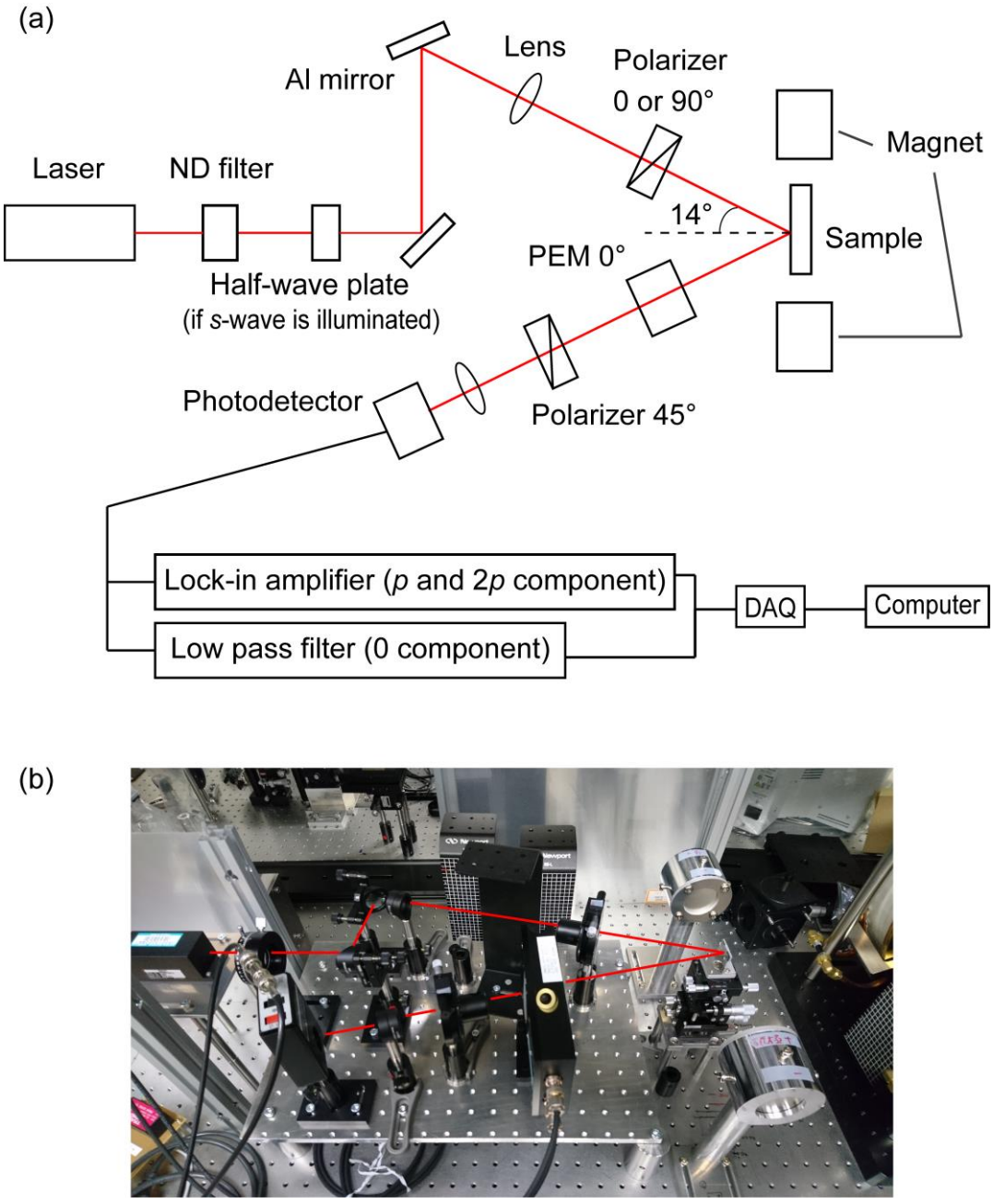

Figure 2-7. (a) Block diagram of L-MOKE measurement system comprising of a polarizer, analyzer, PEM, and a lock-in amplifier. (b) Photograph of actual L-MOKE measurement system constructed in this work. Led line indicates the illumination path.

2.4 L-MOKE response of *s* and *p*-wave in Co thin film and Co nanostructure

In this section, the experimental results of the complex Kerr rotation for *s* and *p*-polarized light in longitudinal configuration are shown in Co thin film and Co nanostructure.

The 20-nm-thick Co thin film was fabricated onto an ITO coated glass substrate by using electron beam evaporation. Co nanostructures were fabricated via electron beam lithography and electron beam evaporation process. The experimental conditions are same as the Au/Co/Au rectangular nanostructure whose fabrication process is described in **Chapter 3**. Co nanostructures consisted of a 20-nm-thick Co thin film, whose long axis length (L_l) is different from the short axis length (L_s). The L_l is 320 nm. The L_s are 115, 140, 160, and 200 nm, respectively. Each rectangular structure was aligned with a spacing of 200, 220, 290, and 340 nm in the short axis direction, and 580 nm in the long axis direction. The device area was 500 × 500 μm^2.

The transmittance spectra in the fabricated Co nanostructure is shown in Fig. 2-8. When the polarization direction of incident light is parallel to the short axis in the structure, it is defined as “V-pol.”, and if the polarization direction is parallel to the long axis, it is defined as “H-pol.”. In V-pol. and H-pol. condition, the typical absorption peak was not observed in the visible region, which means that localized plasmon resonance was not excited in the given wavelength range. In the Co thin film, as shown in Fig. 2-9, no absorption peak was observed in the transmittance spectra in the wavelength range from 500 to 900 nm; therefore, confirming that there is no localized plasmon excitation in Co

thin film in the visible region.

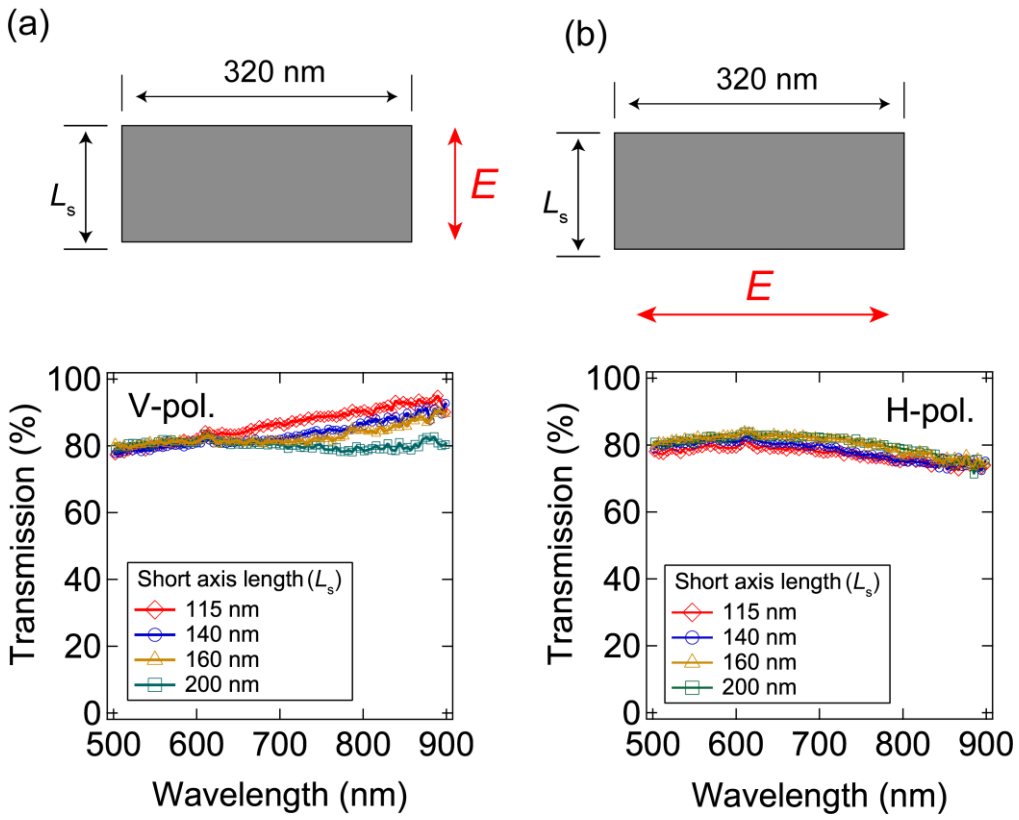

Figure 2-8. Transmittance spectra in rectangular-shaped Co nanostructure in visible region. The polarization direction of the incident light is parallel to (a) the short axis, and (b) the long axis of the nanostructure.

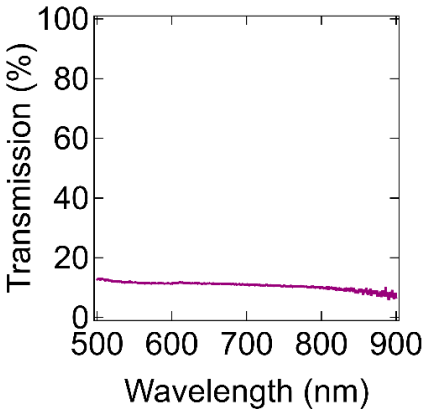

Figure 2-9. Transmittance spectra in 20-nm-thick Co thin film in visible region.

The L-MOKE response in Co thin film is evaluated. Table 1 indicates the L-MOKE activity of *s*-wave and *p*-wave in the Co thin film. The complex Kerr rotation Φ is defined as

$$\Phi = \theta_k + i\eta_k, \tag{2.34}$$

where θ_k and η_k are Kerr rotation, and Kerr ellipticity, respectively [2.8].

Table 1. The longitudinal magneto-optical Kerr effect (L-MOKE) activity in 20-nm-thick Co thin film with respect to the *s*-wave and *p*-wave.

Polarization	Kerr rotation θ_k (mdeg.)	Kerr ellipticity η_k (mdeg.)	Complex Kerr rotation $\lvert\Phi\rvert$ (mdeg.)
s-wave	12.6 ± 0.1	17.3 ± 0.1	21.5 ± 0.1
p-wave	11.7 ± 0.1	16.5 ± 0.1	20.2 ± 0.1

From the table 1, the ratio of $|\Phi|$ for *s*-wave ($|\Phi_s|$) and $|\Phi|$ for *p*-wave ($|\Phi_p|$) ($|\Phi_s|$ /

$|\Phi_p|$) is estimated to be 1.06, whose value is 7 % higher than the theoretical value estimated in **section 2.3.1**. I consider that this difference is due to the measurement accuracy of measurement instruments in my system such as the lock-in amplifier. From this result, the measurement error of $|\Phi_s|$ / $|\Phi_p|$ is estimated to be within 7 %.

G. X. Du, et al., reported that the faraday effect (magneto-optical effect in transmission light) response is different for the polarization direction of incident light in an elliptical nanocylinder shaped magnetic thin film, which is described as a shape anisotropy [2.9]. The absolute value of the complex Kerr rotation for the polarized light, whose polarization direction is perpendicular to the long axis of the nanocylinder, is higher than when the polarization direction is parallel to the long axis. They also suggested that shape anisotropy induced MO activity enhancement increases with increasing aspect ratio of the nanocylinder [2.9]. In order to examine the shape anisotropy dependence of the L-MOKE response in the Co rectangular nanostructure, $|\Phi|$ of the fabricated Co nanostructure with different polarization light was evaluated. Note that the magnetic field was applied parallel to the long axis of the rectangular nanostructure. The plane of incidence was also set parallel to the long axis of rectangular array. $|\Phi|$ for the *s*-wave ($|\Phi_{\mathrm{Co},s}|$) and $|\Phi|$ for the *p*-wave ($|\Phi_{\mathrm{Co},p}|$) with respect to L_s in the Co nanostructures with varying L_s is shown in Fig. 2-10 (a). When the L_s increased, both $|\Phi_{\mathrm{Co},s}|$ and $|\Phi_{\mathrm{Co},p}|$ increased. Figure 2-10 (b) shows the ratio of $|\Phi_{\mathrm{Co},s}|$ to $|\Phi_{\mathrm{Co},p}|$ ($|\Phi_{\mathrm{Co},s}|$ / $|\Phi_{\mathrm{Co},p}|$) as a function of L_s. Although $|\Phi_{\mathrm{Co},s}|$ / $|\Phi_{\mathrm{Co},p}|$ gradually increased with increasing L_s, the values are within the 7% measurement error range determined in the preceding paragraph. Therefore, I concluded that the shape anisotopy induced L-MOKE enhancement can be ignored in the fabricated Co nanostructure.

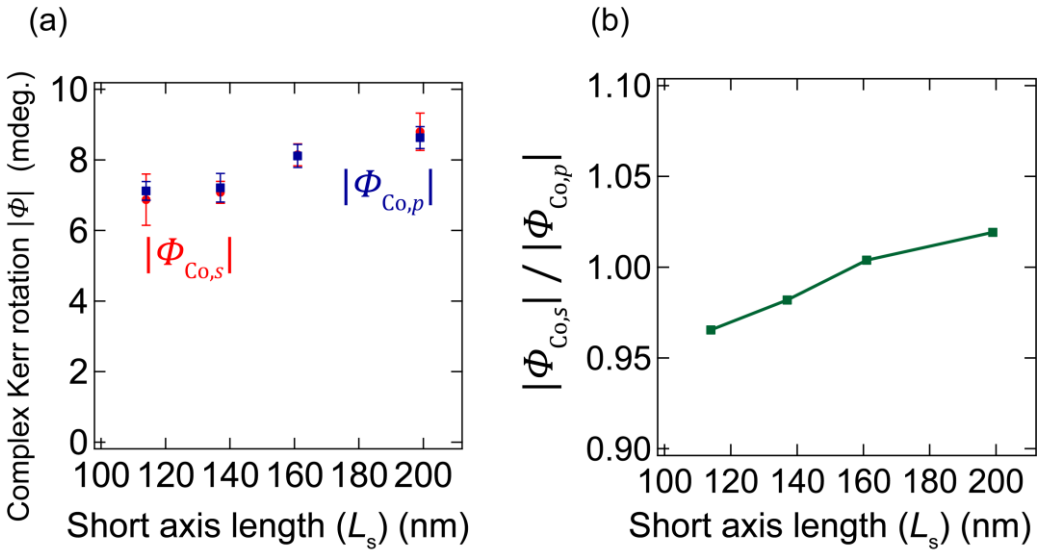

Figure 2-10. (a) The amplitude of the complex Kerr rotation ($|\Phi|$) for *s*-wave ($|\Phi_{Co,s}|$) and *p*-wave ($|\Phi_{Co,p}|$), and (b) the ratio of $|\Phi_{Co,s}|$ to $|\Phi_{Co,p}|$ ($|\Phi_{Co,s}| / |\Phi_{Co,p}|$) with respect to the short axis length (L_s) of the fabricated rectangular-shaped Co nanostructure.

2.5 References

2.1. G. Armelles, A. Cebollada, A. Garcia-Martin, and M. U. Gonzalez, Advanced Optical Materials **1**, 10 (2013).

2.2. J. Zak, E. R. Moog, C. Liu, and S. D. Bader, Physical Review B **43**, 6423 (1991).

2.3. M. F. G. Wood, X. Guo, and A. I. Vitkin, Journal of Biomedical Optics **12**, 014029 (2007).

2.4. K. Sato, Japanese Journal of Applied Physics **20**, 2403 (1981).

2.5. S. N. Jasperson, and S. E. Schnatterly, Review of Scientific Instruments **40**, 761 (1969)

2.6. C. You, and S. Shin, Applied Physics Letters **69**, 1315 (1996).

2.7. P. B. Johnson, and R. W. Christy, Physical Review B **9**, 5056 (1974).

2.8. J. F. Dillon, E. M. Gyorgy, F. Hellman, L. R. Walker, and R. C. Fulton, Journal of Applied Physics **64**, 6098 (1988).

2.9. G. X. Du, T. Mori, S. Sato, and M. Takahashi, Physical Review B Rapid communication **82**, 161403 (2010).

Chapter 3

Enhancement of longitudinal magneto-optical Kerr effect in rectangular-shaped Au/Co/Au nanostructure by localized surface plasmon resonance [3.1]

3.1 Introduction

The magneto-optical (MO) effect, namely, the Kerr effect or the Faraday effect, has gained much attention owing to its capability of manipulating the polarization state of light. Actually, the MO effect has already been applied to various photonic devices such as isolator [3.2], high-resolution MO spatial light modulator [3.3 - 3.4], temperature sensor [3.5], and magneto-optically controlled laser device [3.6]. However, the angle of polarization rotation by the MO Kerr effect (MOKE) is usually very small, around 1.0˚, while practical MO devices demand a larger polarization angle rotation. Therefore, the enhancement of the MO effect is strongly desired.

Recently, several research groups reported that a large MO effect was observed at the resonant wavelength of local-mode surface plasmons (LSPs) [3.7 - 3.17]. This phenomenon has been studied in several ferromagnetic materials such as yttrium iron garnet (YIG) incorporating Au particles [3.7], Au/$[Co/Pt]_n$/Au [3.8, 3.9], Ni nanodisk [3.10 - 3.12], CoPt-Ag nanostructure [3.13], and Au/Co/Au nanostructure [3.14 - 3.17]. Now, this research field is known as “magneto-plasmonics” [3.18 - 3.19]. In previous reports, the authors just measured the wavelength dependence of MOKE and showed that

its peak wavelength was the same as the peak of the transmission/reflection spectrum of the device. However, since MOKE has wavelength dependence [3.20], it is not enough to only show the relationship between plasmon excitation and the enhancement of MOKE without switching the plasmon resonance on and off in the same device. Moreover, from a practical point of view, the figure of merit (FOM) is also important to compare the polarization angle change in MOKE devices [3.21 - 3.23]. FOM is often used to evaluate the performance of magneto-optical device since high FOM gives rise to the signal-to-noise ratio of MO signal [3.21 - 3.22]. So far, the quantitative evaluation of the FOM parameter has not been performed to systematically discuss the effectiveness of plasmon excitation in MOKE devices.

In this section, Au/Co/Au multilayered nano rectangular patch arrays were designed and fabricated on a glass substrate. Since the nano rectangular shape is geometrically anisotropic, the LSP resonance can be switched on or off by simply changing the polarization direction of the incident light at a certain wavelength. Using this structure, the behavior of the longitudinal MOKE (L-MOKE) for different incident polarization directions was examined at an incident angle of 14°, in which angle polarization dependence of L-MOKE is negligible. The FOMs in Au/Co/Au multilayered structures and bare Co nanostructures with the same geometry were also evaluated and compared.

3.2 Sample preparation and experimental method

In this study, a rectangular-shaped Au/Co/Au nanostructures was fabricated. In this section, the fabrication procedure is briefly explained. The fabrication process is shown in Fig. 3-1.

(1) Fabrication of nano patterns onto substrate

The device fabrication process started with cleaning the ITO-coated glass substrate (size: 24 × 24 mm^2) in an ultrasonic bath for 10 min. in different solvents; first in ultrapure water, second in acetone followed by isopropanol (IPA) and finally again in ultrapure water. After the cleaning process, 140-nm-thick positive-type EB resist (ZEON, ZEP520A) was spin coated onto the substrate. Next, the resist-coated substrate was set into the electron beam lithography system (ELIONIX INC., ELS-7700H). Nano patterns were drawn on the resist film at an acceleration voltage of 100 kV, a beam current of 100 pA, and dose shift of 1.6 μsec. The drawing area was 500 × 500 μm^2. After drawing, patterns were developed in a solvent (Tokyo chemical industry, 4-Methyl-2-pentanone) for 2 minutes.

(2) Fabrication of Au/Co/Au nanostructure

After patterning, the substrate with nano patterns was set into an evaporator (Katagiri engineering, EB-Evap) capable of both electron beam deposition (EBD) and thermal deposition (TD). A 5-nm-thick chromium (Cr) thin film was first deposited as an adhesion layer for the Au film via TD and then the 30-nm-thick Au, 6-nm-thick Co, and again 30-nm-thick Au thin films were deposited by EBD without breaking the vacuum condition.

The deposition rate was adjusted to 0.5 Å / s in all films. After deposition, the remaining resist was removed by anisole in an ultrasonic bath and finally rinsed in ultrapure water for 1 minute.

Au/Co/Au rectangular patch arrays with various short axis lengths (L_s = 125, 145, 200 and 245 nm) and fixed long axis length (L_l) of 320 nm were made on the substrate. Figure 3-2 (a) shows the schematic of the thin films' stacking structure. Figure 3-2 (b) - (e) show the scanning electron microscope (SEM) images of the fabricated nanostructures. Each rectangular patch array was aligned with a spacing of 200, 230, 330 and 380 nm in the short axis direction, and 580 nm in the long axis direction. Since the ratios between the length of the rectangular patch and spacing for all devices were kept almost at the same value, the total area covered by nanostructures is approximately equalized.

Absorption properties of the structures were characterized by measuring the transmittance spectra using a microspectrophotometer. This system consists of a microscope (Olympus, BX51) and a spectrometer (Ocean optics, USB2000+XR1-ES), which is capable of spectroscopic measurements in the wavelength range from 500 to 900 nm. The polarization direction of the incident light was changed by rotating the polarizer that was set in the path of the beam between the sample and the light source. All samples were measured with the incident beam perpendicular to the sample plane.

MO properties were measured via an L-MOKE measurement system introduced in **Chapter 2**. A diode laser with wavelength (λ) of 785 nm and linearly polarized was used as a light source. Laser light was collimated and introduced at the device surface at a fixed

incident angle of 14 degrees. As shown in Fig. 3-3, the plane of incidence was set parallel to the long axis of the rectangular structure. In the optical setup, a half waveplate was introduced in the light path and, by rotating the polarizer, the polarization direction of the incident light was changed between *p*-pol. and *s*-pol. to switch the surface plasmon resonance on or off. An external magnetic field (*H*) of 1000 Gauss was applied parallel to the long axis of the structure. Both Kerr rotation and Kerr ellipticity were saturated for all devices when the *H* was applied parallel to the long axis of the structure above 900 Gauss. Thus, 1000 Gauss is enough to measure the saturated values of Kerr rotation and ellipticity.

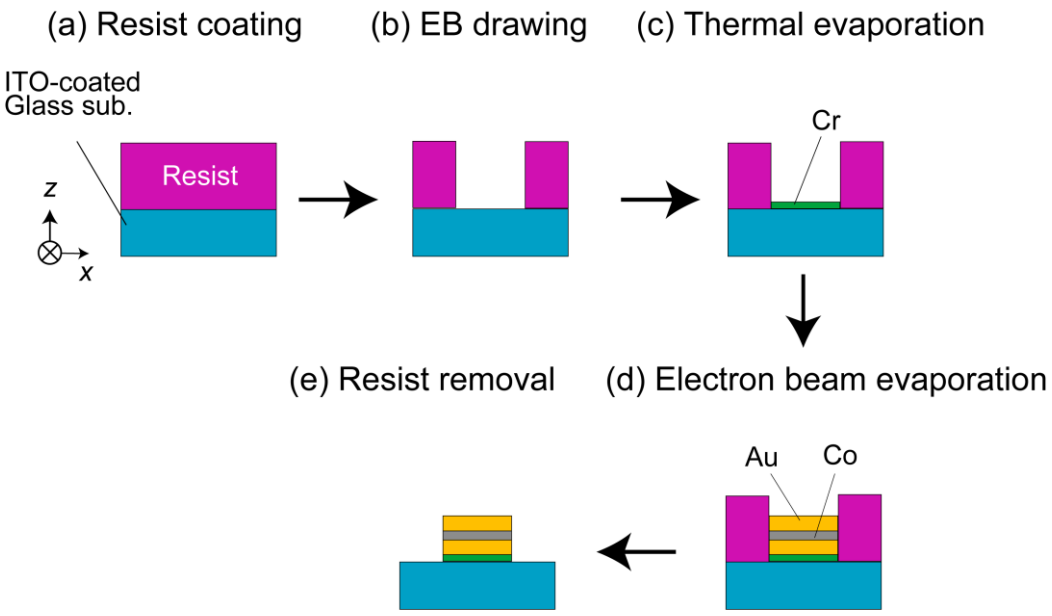

Figure 3-1. Fabrication process of Au/Co/Au nanostructures. (a) positive-type EB resist was coated onto ITO-coated glass substrate. (b) nano patterns were drawn on the resist film using EB lithography. After drawing, patterns were developed. (c) Cr adhesion layer was fabricated using thermal evaporation. (d) Au, Co, and Au layer were fabricated via electron beam evaporation. (e) the remaining resist was removed.

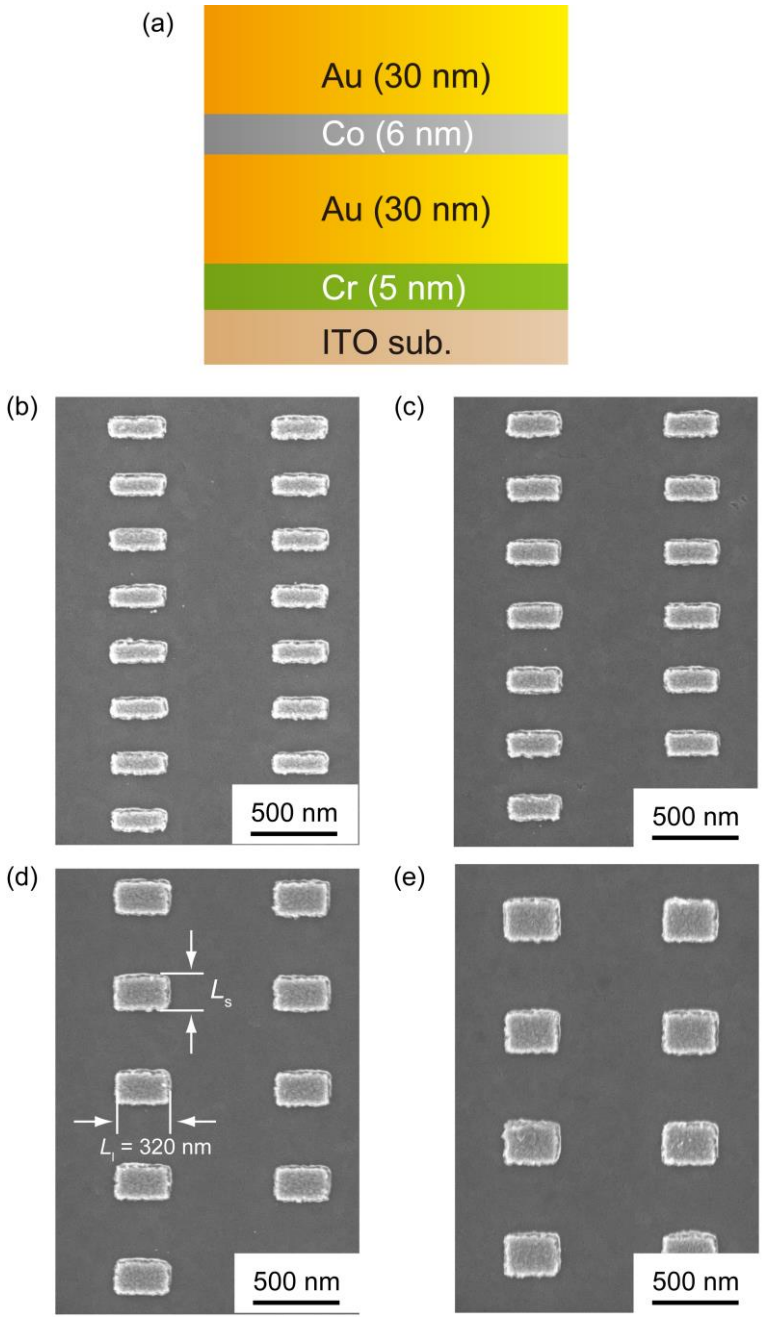

Figure 3-2. (a) Cross-sectional illustration of the thin films' stacking structure. SEM images of the Au/Co/Au nanostructures with a fixed long axis length (L_l) of 320 nm and various short axis lengths (L_s) of (b) 125 nm, (c) 145 nm, (d) 200 nm, and (e) 245 nm. (Copyright (2018) The Japanese Society of Applied Physics.)

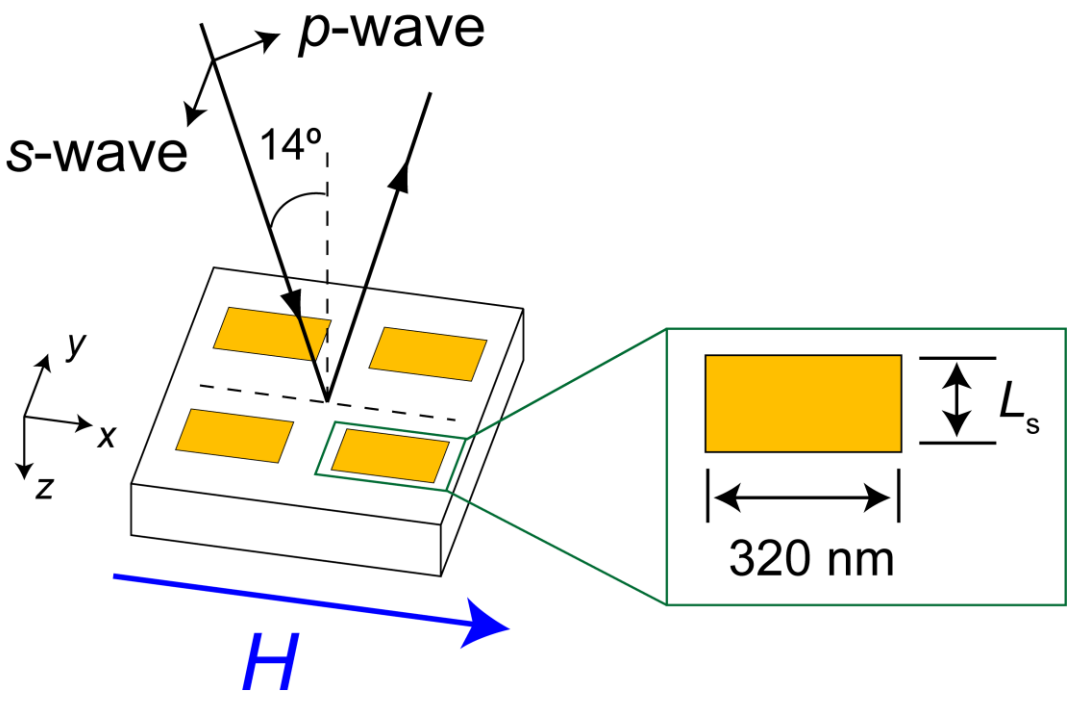

Figure 3-3. Illustration of the L-MOKE measurement setup. Magnetic field (*H*) is applied parallel to the long axis of the nanostructures and the plane of incident.

3.3 Transmission spectra in Au/Co/Au rectangular nanostructure

Transmittance spectra of the fabricated multilayered Au/Co/Au rectangular patch array is shown in Fig. 3-4. There are two measurement conditions: (1) the polarization direction of the incident light is set parallel to the short axis – defined as "V-pol." and (2) the polarization direction of the incident light is set parallel to the long axis – defined as "H-pol.". Under the V-pol. condition, transmission peaks, marked by arrows in Fig. 3-4 (a), gradually shifted to longer wavelength as L_s increased. In the case of L_s=200 nm, a transmission peak appeared at λ = 810 nm, which is closest to the laser wavelength of the L-MOKE system. On the other hand, under the H-pol. condition (Fig. 3-4 (b)), no transmission peaks were observed in the visible region. From these results, the wavelength of the SP resonance can be tuned by changing the lengths of the rectangular patch and polarization control enables us to switch the LSP resonance on and off.

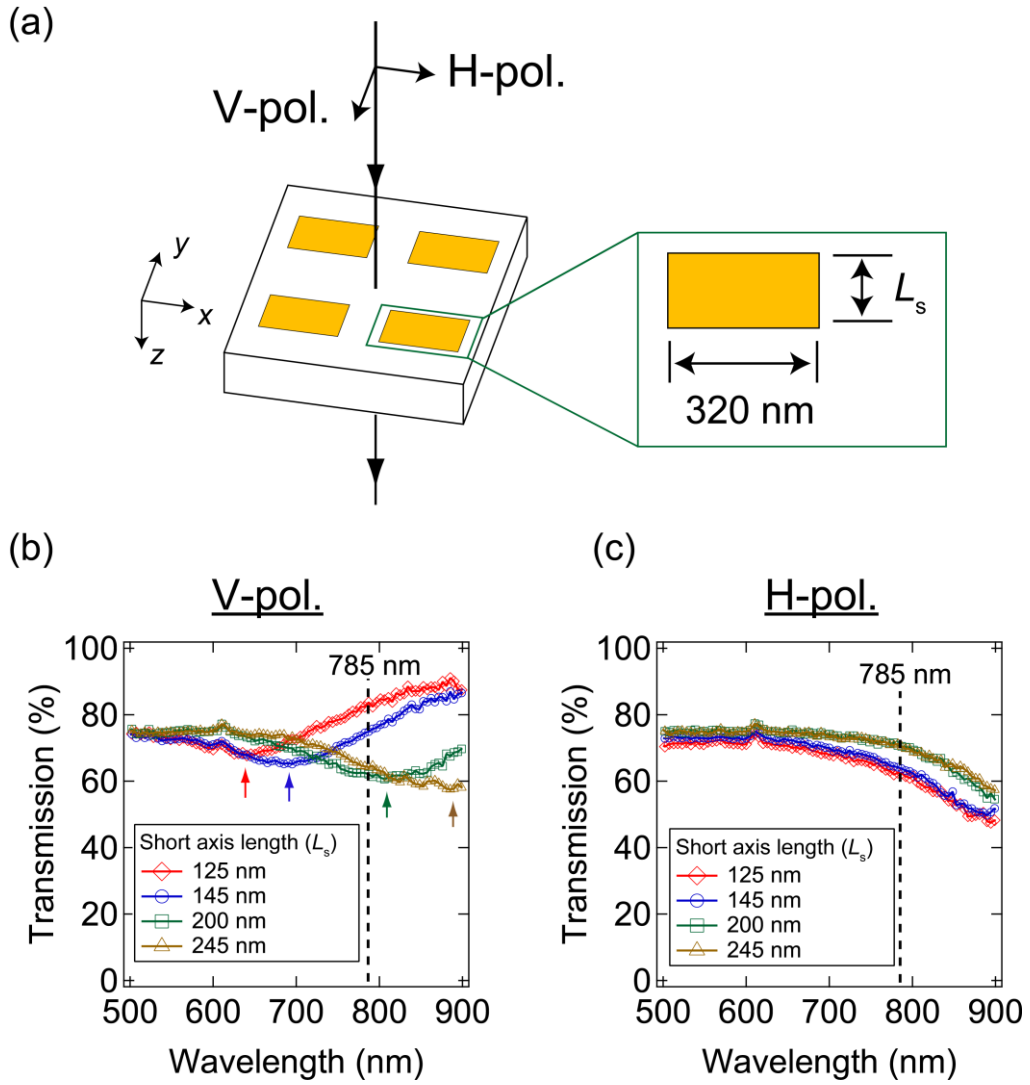

Figure 3-4. (a) Illustration of the transmission spectra measurement setup. The incident beam is perpendicular to the sample plane. Transmission spectra of Au/Co/Au nanostructures with different short axis lengths (L_s = 125, 145, 200, and 245 nm) when (b) the polarization direction of incident light is along the short axis of the nanostructure (V-pol.) and (c) the polarization direction of incident light is along the long axis of the nanostructure (H-pol.). (Copyright (2018) The Japanese Society of Applied Physics.)

3.4 L-MOKE activity in Au/Co/Au rectangular nanostructure under localized surface plasmon excitation

The L-MOKE activity in the fabricated Au/Co/Au nano rectangular arrays was evaluated. Figures 3-5 (a) and (b) show the Kerr rotation (θ) and Kerr ellipticity (η), respectively, for varying L_s. Both θ and η take a maximum value at L_s = 200 nm under V-pol. illumination. Figure 3-5 (c) shows the relationship between the absolute value of the complex Kerr rotation ($|\Phi|$) and L_s, where the complex Kerr rotation is defined as,

$$\Phi = \theta + i\ \eta \text{ [3.24].} \tag{3.1}$$

As shown in Fig. 3-5 (c), $|\Phi|$ for V-pol. ($|\Phi_{\text{V-pol.}}|$) is always larger than H-pol. ($|\Phi_{\text{H-pol.}}|$). While $|\Phi_{\text{H-pol.}}|$ shows an almost constant value regardless of L_s, $|\Phi_{\text{V-pol.}}|$ varies according to the L_s and becomes maximum at L_s = 200 nm, in which the LSPs are excited at the laser wavelength. Figure 3-5 (d) shows the ratio of $|\Phi_{\text{V-pol.}}|$ to $|\Phi_{\text{H-pol.}}|$ ($|\Phi_{\text{V-pol.}}| / |\Phi_{\text{H-pol.}}|$) as a function of L_s. It is clear that the ratio becomes maximum at L_s = 200 nm, which means the largest MOKE occurs at this L_s. In **Chapter 2**, it was shown that the polarization dependence of L-MOKE can be negligible at the incident angle of 14˚ via experiment using the rectangular-shaped Co nano patch array. From these results, I confirmed that the strong enhancement of L-MOKE comes from the LSP resonance in the Au nano structures. These results indicate that there is a relationship between the plasmon excitation and magneto-optical effect enhancement.

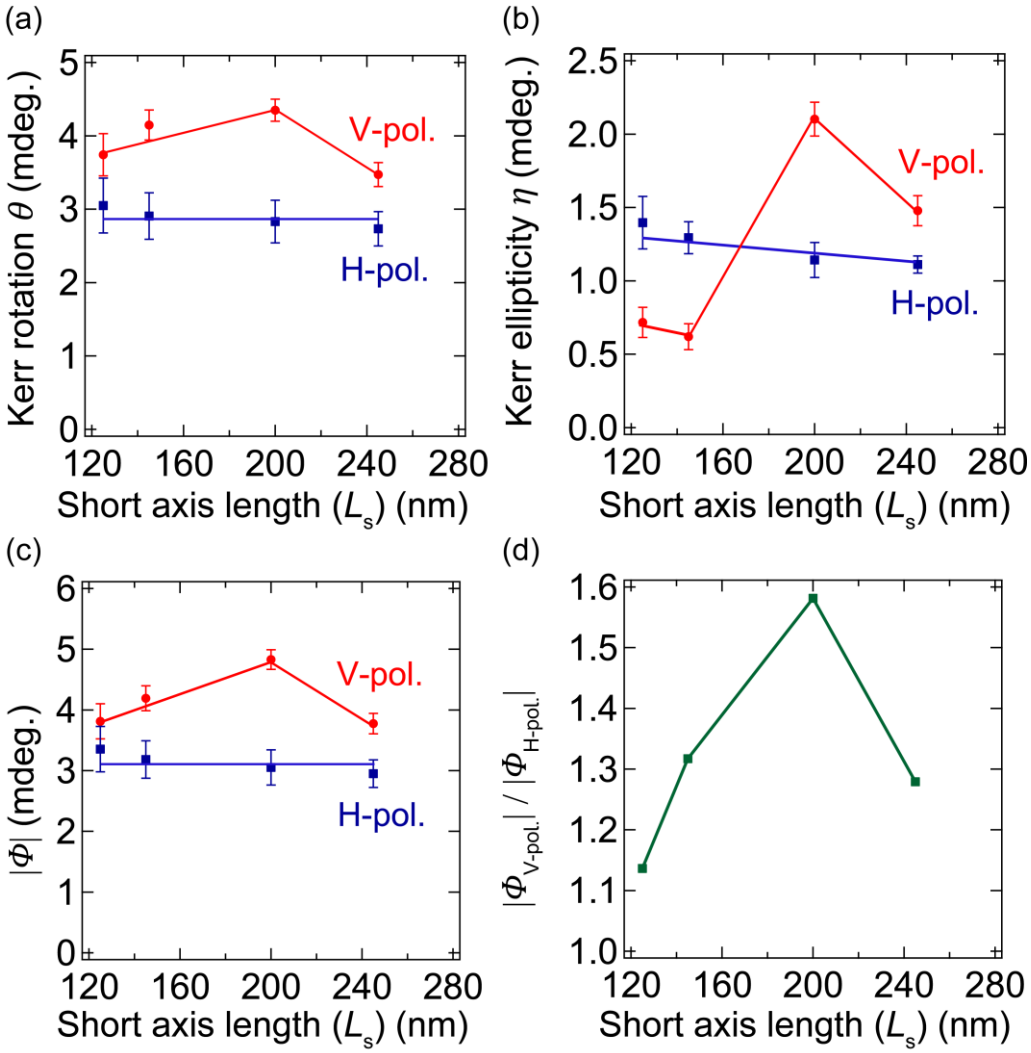

Figure 3-5. (a) The Kerr rotation (θ), (b) the Kerr ellipticity (η), and (c) absolute values of complex Kerr rotation angle ($|\Phi|$) in Au/Co/Au nanostructures for polarized light along the short axis of the nanostructure (V-pol., $|\Phi_{\text{V-pol.}}|$, red circle) and along the long axis of the nanostructure (H-pol., $|\Phi_{\text{H-pol.}}|$, blue square) with respect to the short axis length (L_s) of the Au/Co/Au nanostructures. (d) The ratio of $|\Phi_{\text{V-pol.}}|$ to $|\Phi_{\text{H-pol.}}|$ ($|\Phi_{\text{V-pol.}}| / |\Phi_{\text{H-pol.}}|$) as a function of L_s of the nanostructures. (Copyright (2018) The Japanese Society of Applied Physics.)

3.5 Light power dependence of L-MOKE activity in Au/Co/Au rectangular nanostructure under localized surface plasmon excitation

Figures 3-6 (a), (b), and (c) show the light power (P) dependence of Kerr rotation (θ_{wLSPs}), Kerr ellipticity (η_{wLSPs}) and the absolute value of the complex Kerr rotation ($|\Phi_{\mathrm{wLSPs}}|$), respectively, under V-pol. illumination in an rectangular-shaped Au/Co/Au nanostructure, whose L_s is 200 nm. In this experimental condition, LSP resonance was excited in the Au/Co/Au nanostructure. As shown in Fig. 3-6, θ_{wLSPs}, η_{wLSPs}, and $|\Phi_{\mathrm{wLSPs}}|$ take an almost constant value regardless of P in the range from 20 to 80 mW. Hence, significant MOKE activity increase was not observed by increasing the light power. The electric field intensity ($|E|$) generated by the LSP resonance is proportional to the square root of the light power of incident light [3.25]. Therefore, in this case, the Co layer would experience twice the amount of the electric field when the light power is raised from 20 to 80 mW. However, from these results, it is not clear if the electric field induced by LSP resonance is related to the L-MOKE activity enhancement.

Next, the results from the point of view of plasmon resonance induced light absorption are discussed. When LSP resonance is excited in a nanostructure, a temperature increase is caused by optical heating arising from the strong light absorption [3.26]. Moreover, this temperature increase is proportional to the power of incident light [3.27]. Therefore, in the case of the Au/Co/Au nanostructures in this study, the temperature will increase 4 times when increasing the P from 20 to 80 mW. By raising the temperature, MOKE activity would become weak because MOKE activity is related to the magnetization in the substance [3.18], which is decreases with increasing temperature [3.28]. However, the

results demonstrated that the MOKE activity was kept constant in the range of 20 to 80 mW, suggesting that the plasmonic enhancement of L-MOKE overcomes the degradation of L-MOKE activity by optical heating.

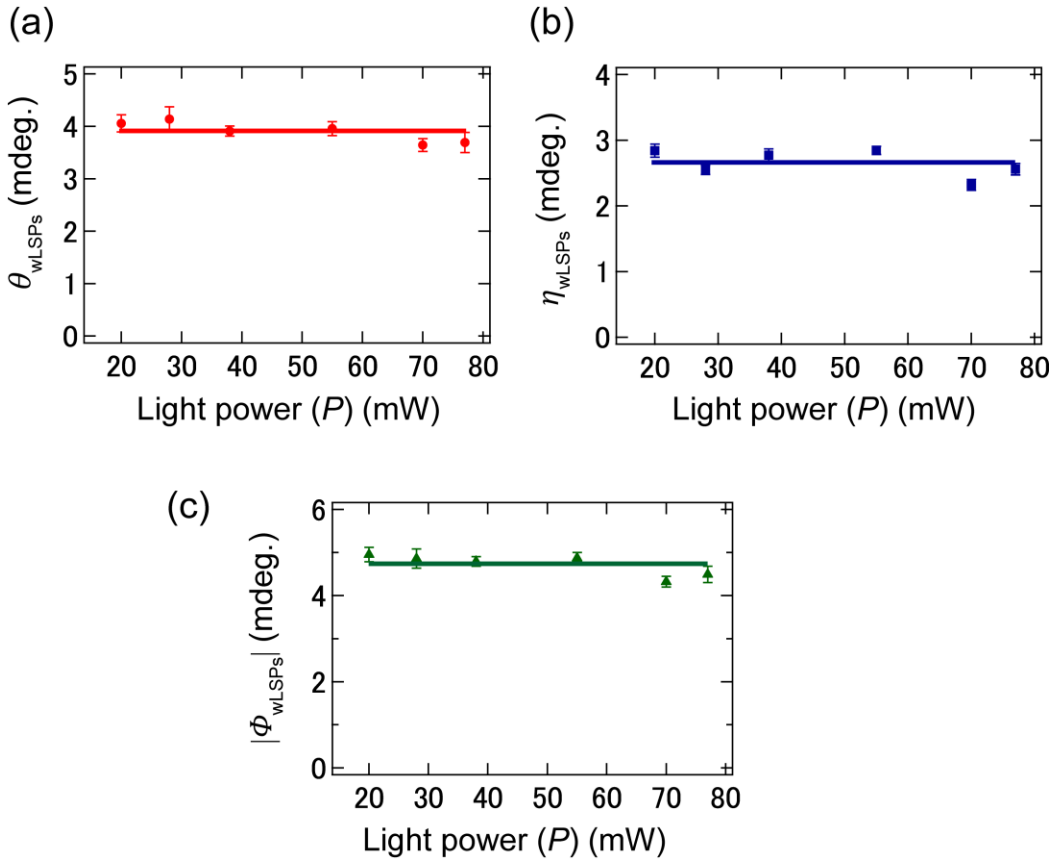

Figure 3-6. The light power (P) dependence of (a) the Kerr rotation (θ_{wLSPs}), (b) the Kerr ellipticity (η_{wLSPs}), and (c) the absolute values of the complex Kerr rotation angle ($|\Phi_{wLSPs}|$) in Au/Co/Au nanostructures (L_s = 200 nm) when the polarization of the incident light is along the short axis of the nanostructure.

3.6 Magneto-optical FOM evaluation in Au/Co/Au nanostructure

As stated in **section 3.1**, magneto-optical FOM is used to assess the efficiency of the magneto-optical device. In order to evaluate the magneto-optical FOM, first, the reflectivity (R) of the fabricated Au/Co/Au devices were measured at λ = 785 nm. As shown in Fig. 3-7 (a), R for H-pol. ($R_{\text{H-pol.}}$) gradually decreased with increasing L_s. On the other hand, R for V-pol. ($R_{\text{V-pol.}}$) reached its maximum at L_s = 200 nm. Next, the magneto-optical FOM was estimated. According to References 3.21, 3.22, and 3.29, the FOM of an MO device is defined as

$$FOM = \sqrt{R} \times \theta. \tag{3.2}$$

Afterwards FOM value of the devices were plotted with respect to L_s in Fig. 3-7 (b). As shown in Fig. 3-7 (b), FOM in H-pol. ($FOM_{\text{H-pol.}}$) gradually decreased with increasing L_s. However, the FOM in V-pol. ($FOM_{\text{V-pol.}}$) takes a maximum value at L_s = 200 nm, similar to the L-MOKE results in **section 3.4**. Moreover, at L_s = 200 nm, $FOM_{\text{V-pol.}}$ becomes approximately 1.8 times larger than $FOM_{\text{H-pol}}$. This result indicates that the excitation of LSPs on Au layer improves the FOM of the device.

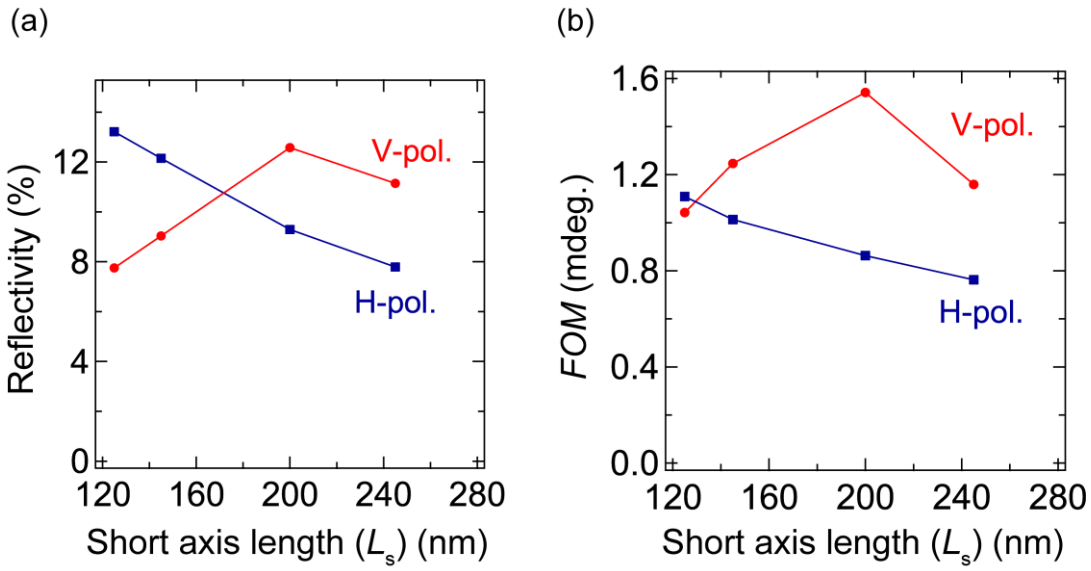

Figure 3-7. (a) The reflectivity and (b) the FOM parameters of Au/Co/Au nanostructures with respect to L_s of the Au/Co/Au nanostructures when incident light polarization is along the short axis of the nanostructure (V-pol., red circle) and along the long axis of the nanostructure (H-pol., blue square). (Copyright (2018) The Japanese Society of Applied Physics.)

3.7 Comparison of the magneto-optical FOM between Au/Co/Au plasmonic nanostructure and Co nanostructure

In order to verify the effect of the Au layer on the Co layer properly, especially regarding the MO activity and the FOM, a bare Co rectangular nanostructure was fabricated. 6-nm-thick Co nano rectangular patches were made on an ITO glass substrate. The geometries of the structures are the same as Au/Co/Au structure, whose dimensions are 200 nm × 320 nm. Figure 3-8 shows the transmittance spectra in the 6-nm-thick Co nanostructure. In both V-pol. and H-pol. measurements, no absorption peak was observed at the visible region for the Co nanostructures, which means there was no plasmon excitation in the given wavelength range. Hence, the absorption dips shown in Fig. 3-4 (a) originated from the Au layers were reconfirmed.

In addition, the $|\Phi|$ for V-pol. ($|\Phi_{\text{Co, V-pol.}}|$) and $|\Phi|$ for H-pol. ($|\Phi_{\text{Co, H-pol.}}|$) were measured in the Co structure as 2.1 mdeg. and 2.3 mdeg., respectively. Since the values of $|\Phi_{\text{Co, V-pol.}}|$ and $|\Phi_{\text{Co, H-pol.}}|$ are almost the same, the L-MOKE response in the Co structure is independent of the polarization direction, and it implies that the enhancement of $|\Phi|$ in the multilayered nanostructure shown in Fig. 3-5 (c) originated from the Au layer.

Next, the FOM parameters of the Au/Co/Au and the bare Co nanostructures were compared. The R in the Co nanostructure for V-pol. and H-pol. are 5.0 % and 4.6 %, which are about half of the R of the non-LSP-resonant Au/Co/Au nanostructure. The FOMs for Co nanostructures are 0.34 mdeg. for H-pol. and 0.45 mdeg. for V-pol. conditions. Figure 3-9 shows the summary of the comparison of FOM values in the

Au/Co/Au and the Co nanostructures (L_s =200 nm) with V- and H-pol. excitation. The FOM of the Au/Co/Au nanostructure for V-pol. is about 3.8 times higher than that of the Co nanostructure. This indicates that Au/Co/Au nano rectangular patch array with LSP excitation is the most superior to other Co devices without LSP excitation in terms of FOM. These results demonstrate that the addition of a plasmonic Au layer to the magnetic active Co layer is an effective way to enhance not only MO activity but also the FOM. This knowledge could promote the development of submicron-scaled MO devices such as a magneto-optical spatial light modulator for realizing holographic 3D movies [3.30, 3.31].

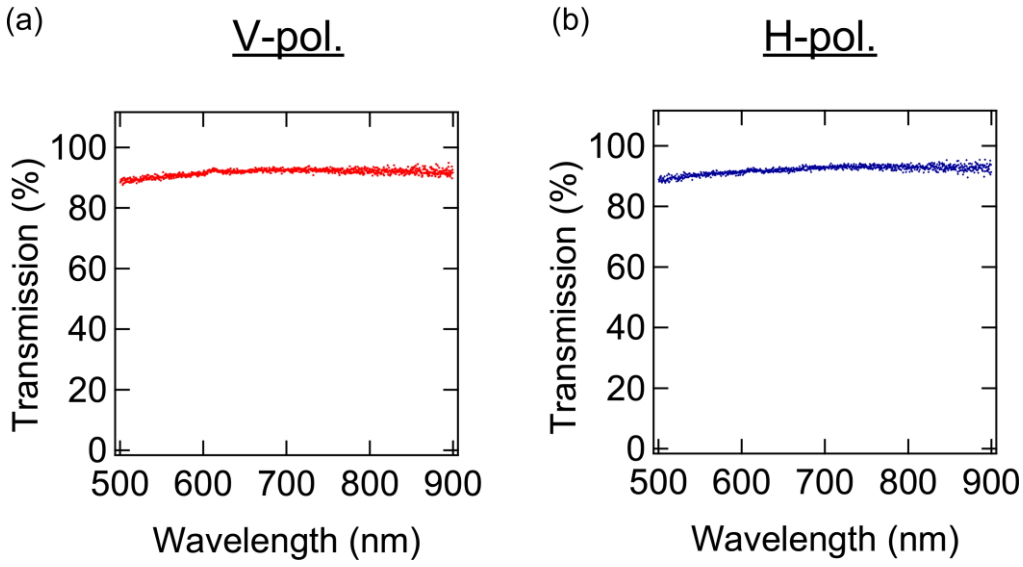

Figure 3-8. Transmission spectra of 6-nm-thick Co nanostructures, whose dimensions are 200 nm × 320 nm. (a) The polarization direction of incident light is along the short axis of the nanostructure (V-pol.). (b) The polarization direction of incident light is along the long axis of the nanostructure (H-pol.).

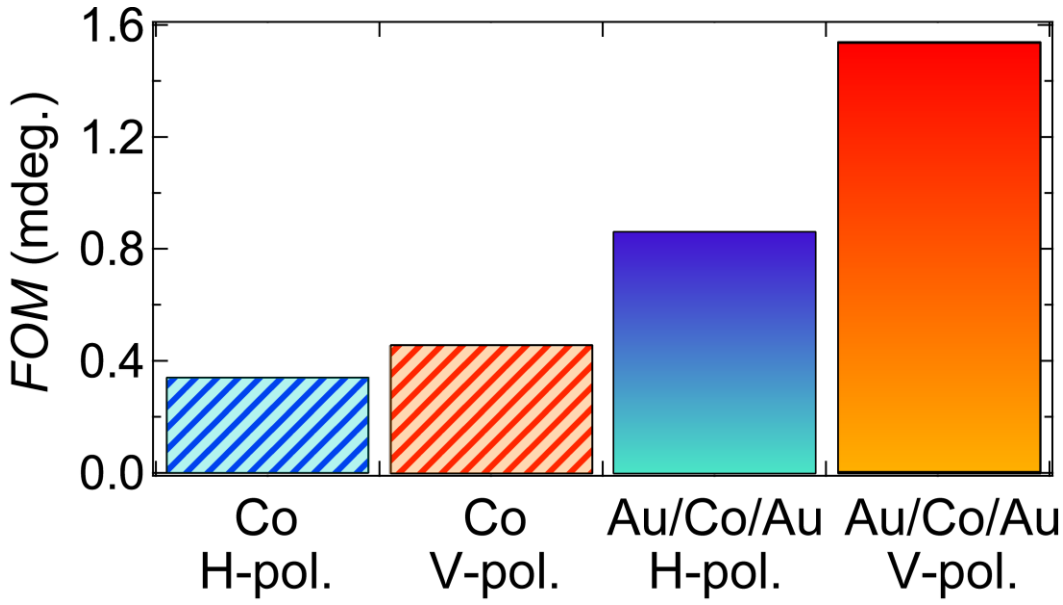

Figure 3-9. FOM parameter for H-pol. and V-pol. in Co and Au/Co/Au nanostructure, whose dimensions are 200 nm × 320 nm.

3.8 References

3.1. **Y. Kikuchi**, and T. Tanaka, Japanese Journal of Applied Physics Rapid Communication **57**, 110305 (2018).

3.2. W. Van Parys, B. Moeyersoon, D. Van Thourhout, R. Baets, M. Vanwolleghem, B. Dagens, J. Decobert, O. Le Gouezigou, D. Make, R. Vanheertum, and L. Lagae, Applied Physics Letters **88**, 071115 (2006).

3.3. J. Park, J. Y. Cho, K. Nishimura, and M. Inoue, Japanese Journal of Applied Physics **41**, 1813 (2002).

3.4. K. Aoshima, K. Machida, D. Kato, T. Mishina, K. Wada, Y. F. Cai, H. Kinjo, K. Kuga, H. Kikuchi, T. Ishibashi, and N. Shimidzu, Journal of Display Technology **11**, 129 (2015).

3.5. M. Kustov, R. Grechishkin, M. Gusev, O. Gasanov, and J. McCord, Advanced Materials **27**, 5017 (2015).

3.6. T. Goto, R. Morimoto, J. W. Pritchard, M. Mina, H. Takagi, Y. Nakamura, P. B. Lim, T. Taira, and M. Inoue, Optics Express **24**, 17635 (2016).

3.7. S. Tomita, T. Kato, S. Tsunashima, S. Iwata, M. Fujii, and S. Hayashi, Physical Review Letters **96**, 167402 (2006).

3.8. G. X. Du, T. Mori, M. Suzuki, S. Saito, H. Fukuda, and M. Takahashi, Applied Physics Letters **96**, 081915 (2010).

3.9. G. X. Du, T. Mori, S. Saito, and M. Takahashi, Physical Review B **82**, 161403 (2010).

3.10. N. Maccaferri, A. Berger, S. Bonetti, V. Bonanni, M. Kataja, Q. H. Qin, S. van Dijken, Z. Pirzadeh, A. Dmitriev, J. Nogues, J. Akerman, and P. Vavassori,

Physical Review Letters **111**, 167401 (2013).

3.11. K. Lodewijks, N. Maccaferri, T. Pakizeh, R. K. Dumas, I. Zubritskaya, J. Akerman, P. Vavassori, and A. Dmitriev, Nano Letters **14**, 7207 (2014).

3.12. I. Zubritskaya, K. Lodewijks, N. Maccaferri, A. Mekonnen, R. K. Dumas, J. Akemaan, P. Vavassori, and A. Dmitriev, Nano Letters **15**, 3204 (2015).

3.13. H. Yamane, K. Takeda, and M. Kobayashi, Applied Physics Letters **106**, 052409 (2015).

3.14. J. B. Gonzalez-Diaz, A. Garcia-Martin, J. M. Garcia-Martin, A. Cebollada, G. Armelles, B. Sepulveda, Y. Alaverdyan, and M. Kall, Small **4**, 202 (2008).

3.15. D. Meneses-Rodriguez, E. Ferreiro-Vila, P. Prieto, J. Anguita, M. U. Gonzalez, J. M. Garcia-Martin, A. Cebollada, A. Garcia-Martin, and G. Armelles, Small **7**, 3317 (2011).

3.16. G. Armelles, A. Cebollada, F. Garcia, A. Garcia-Martin, and N. de Sousa, ACS Photonics **3**, 2427 (2016).

3.17. C. A. Herreno-Fierro, E. J. Patino, G. Armelles, and A. Cebollada, Applied Physics Letters **108**, 021109 (2016).

3.18. G. Armelles, A. Cebollada, A. Garcia-Martin, and M. U. Gonzalez, Advanced Optical Materials **1**, 10 (2013).

3.19. D. Sander, S. O. Valenzuela, D. Makarov, C. H. Marrows, E. E. Fullerton, P. Fischer, J. McCord, P. Vavassori, S. Mangin, P. Pirro, B. Hillebrands, A. D. Kent, T. Jungwirth, O. Gutfleisch, C. G. Kim, and A. Berger, Journal of Physics D-Applied Physics **50**, 363001 (2017).

3.20. K. Sato, H. Hongu, H. Ikekame, Y. Tosaka, M. Watanabe, K. Takanashi and H. Fujimori, Japanese Journal of Applied Physics **32**, 989 (1993).

3.21. T. Kokogawa, T. Numata, and S. Inokuchi, IEEE Transactions on Magnetics **29**, 3808 (1993).

3.22. R. Atkinson, S. Pahirathan, I. W. Salter, P. J. Grundy, C. J. Tatnall, J. C. Lodder, and Q. Meng, Journal of Magnetism and Magnetic Materials **162**, 131 (1996).

3.23. P. Hansen, Journal of Magnetism and Magnetic Materials **83**, 6 (1990).

3.24. J. F. Dillon, E. M. Gyorgy, F. Hellman, L. R. Walker, and R. C. Fulton, Journal of Applied Physics **64**, 6098 (1988).

3.25. K. A. Willets, and R. P.V. Duyne, Annual Review of Physical Chemistry **58**, 267 (2007).

3.26. G. Baffou, R. Quidant, and C. Girard, Applied Physics Letters **94**, 153109 (2009).

3.27. G. Baffou, R. Quidant, and F. J. G. de Abajo, ACS Nano **4**, 709 (2010).

3.28. C. Zener, Physical Review **96**, 1335 (1954).

3.29. W. B. Zeper, A. P. J. Jongenelis, B. A. J. Jacobs, H. W. Vankesteren, and P. F. Carcia, IEEE Transactions on Magnetics **28**, 2503 (1992).

3.30. N. Funabashi, K. Aoshima, K. Machida, K. Kuga, T. Ishibashi, and N. Shimidzu, IEEE Transactions on Magnetics **46**, 1998 (2010).

3.31. K. Aoshima, N. Funabashi, K. Machida, Y. Miyamoto, K. Kuga, T. Ishibashi, N. Shimidzu, and F. Sato, Journal of Display Technology **6**, 374 (2010).

Chapter 4

In-plane magnetic anisotropy energy increase in Au/Co/Au nanostructure by localized surface plasmon resonance [4.1]

4.1 Introduction

Magnetic properties of magnetic devices strongly depend on their base materials, the fabrication process, and the surrounding environments. When we want to modulate the magnetic properties of these devices after they have been made, external stimuli from the environment such as heat, pressure, and so on, are applied [4.2 - 4.4]. In the present, in order to develop ultra-fast magnetic memory devices, several magnetization control techniques have been proposed, including the voltage-driven magnetization switching [4.5 - 4.7], photo-induced magnetization [4.8 - 4.10], and helicity-dependent magnetic switching [4.11 – 4.13]. However, these phenomena are only observed under limited experimental conditions like using ultrathin magnetic film with a thickness below 1 nm [4.5 - 4.7], in ultra-low temperature [4.8 - 4.10], or using a femtosecond pulsed laser irradiation [4.11 – 4.13].

Recently, several groups have reported that the magneto-optical effect is enhanced at the resonant wavelength of the local-mode surface plasmons (LSPs) in metal nanostructures at room temperature [4.14 - 4.18]. This research field is now called as “magneto-plasmonics” [4.19 – 4.20]. As mentioned in **Chapter 3**, I have also observed a similar effect where the L-MOKE and the magneto-optical FOM in an Au/Co/Au nanostructure

are enhanced by the LSP excitation [4.21]. According the recent reports [4.14 - 4.21], the LSPs affect (and modulate) the magneto-optical property of the magnetic thin film, but it still remains undiscussed whether surface plasmon excitation affects the magnetization mechanism or not.

Magnetic anisotropy is an essential factor for practical applications, because it determines the thermal stability of magnetic devices, like magnetic random access memory (MRAM) and magnetic recording devices (e.g. hard disk drive), just to name a few [4.22, 4.23]. In these devices, the magnetic anisotropy usually decreases when the temperature of the material increases. Heat-assisted magnetic recording (HAMR) technology exploits this phenomenon by modulating the magnetic anisotropy through temporary heating of the recording media and then writing tiny (high-density) data bits on the media [4.24, 4.25]. In this section, the first demonstration of the increase of the in-plane magnetic anisotropy in Au/Co/Au nanostructure under LSP resonance is presented. The mechanism behind this increase is also discussed.

4.2 Sample preparation and experimental method

Figure 4-1 (a) shows the schematic illustration of the fabricated nanostructure including a cross section of the thin film's stacking order. An array of these square patch nanostructures (170 × 170 nm^2 in lateral direction) consisting of Cr (5 nm) / Au (30 nm) / Co (6 nm) / Au (t_{Au} = 5, 10, 30 nm) were fabricated on an ITO thin film coated glass substrate using electron beam lithography. The fabrication process and method are same to that of the rectangular-shaped Au/Co/Au nanostructure, described in **Chapter 3**. Figure 4-1 (b) is the SEM image of the fabricated nanostructures. The distance between the center of each structures in the *x* and *y* directions is 480 nm.

The optical properties of the fabricated samples were characterized by measuring the transmission spectra using a UV-visible spectrometer as explained in **Chapter 3**.

The characteristics of the sample structures' magnetic anisotropy at room temperature were evaluated by the magnetic field dependence of the longitudinal and the polar MOKE since (1) the MOKE is a reflection of the magnetization of the material [4.26], and (2) it is almost impossible to directly measure the magnetization loop with a conventional magnetometer due to the very small magnetic moment in the nanostructure. The in-plane magnetization curve was evaluated using my home-built L-MOKE measurement system, whose design and operation details are found in **Chapter 2**. In this experiment, diode lasers with wavelengths of 640 and 785 nm were used as light sources and these laser beams illuminates the sample surface at a fixed incident angle of 14˚ and a polarization sets parallel to the edge of the nanostructure surface. The magnetic field was applied

parallel to the sample surface (Fig. 4-2 (a)). The out-of-plane magnetization curve was evaluated via a polar magneto-optical Kerr effect (P-MOKE) measurement system (NEOARK CORP., MODEL BH-M800UV-HD-10). In this system, a xenon lamp was used as a light source, and the wavelength (λ) of the incident light was selected by a monochromator. Note that it is difficult to carry out a reliable measurement of the P-MOKE loop for wavelengths beyond 800 nm due to the lack of light intensity of incident light. As shown in Fig. 4-2 (b), the plane of incidence was set parallel to the edge of the nanostructure surface. The incident angle was fixed at about 5˚. A magnetic field of ±20 k Gauss was applied perpendicular to the sample plane. In order to obtain high S/N P-MOKE loops for discussing the saturation field change by plasmon resonance, the P-MOKE loops were measured over one hundred times and then were averaged.

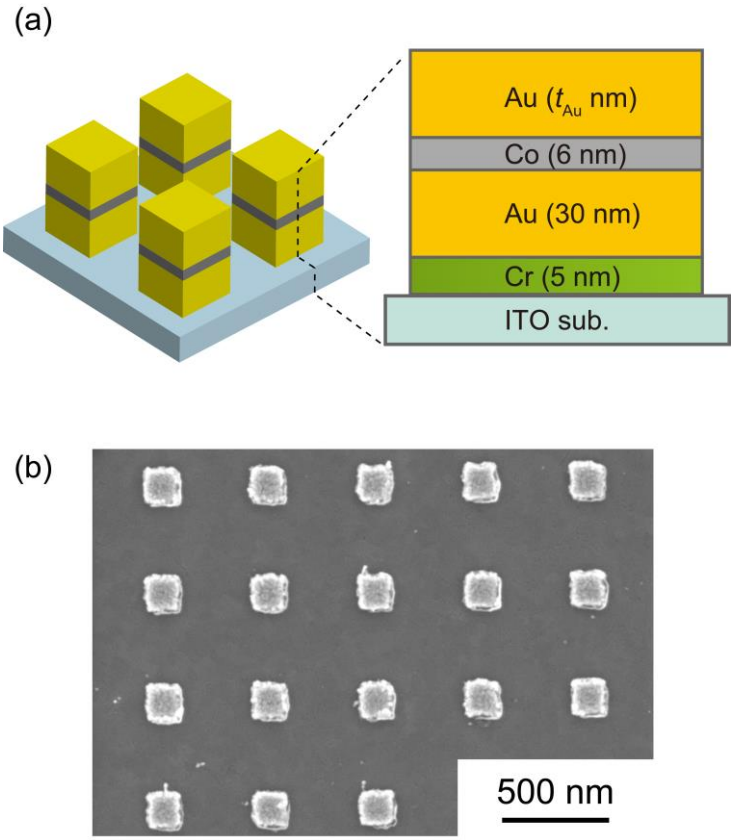

Figure 4-1. (a) Schematic of the fabricated nanostructure and the stacking structure of the thin film (cross-section view). The Au top layer thickness (t_{Au}) is 5, 10, and 30 nm. (b) SEM image of fabricated Au/Co/Au (t_{Au} = 30 nm) nanostructures.

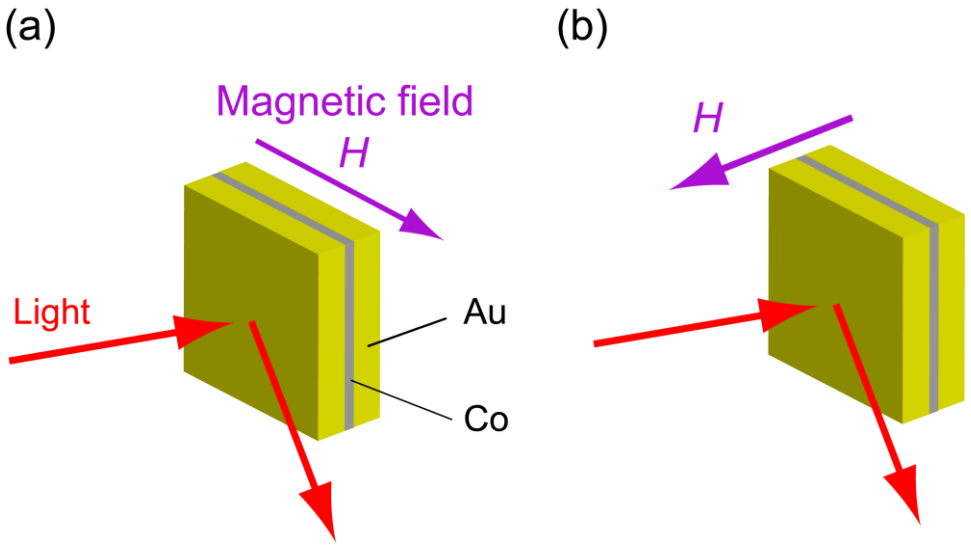

Figure 4-2. (a) L-MOKE and (b) P-MOKE measurement configuration. In L-MOKE, magnetic field (*H*) is applied parallel to the surface of the Au/Co/Au nanostructure. In P-MOKE, *H* is applied perpendicular to the surface of the Au/Co/Au nanostructure.

4.3 Transmission spectra in square-shaped Au/Co/Au nanostructure

To evaluate the plasmonic properties of the fabricated Au/Co/Au (t_{Au} = 30 nm) nanostructure, the transmission spectra was measured as shown in Figure 4-3. The polarization direction of the incident light was parallel to the edge of nano square arrays. From this result, the transmission peak originating from the localized surface plasmon resonance (LSPR) was observed only at λ = 770 nm, and no other absorption peaks were present in the range of λ = 500 to 640 nm. Therefore, LSP excitation can be switched on or off by changing the wavelength of the incident light, which is why, for the L-MOKE and P-MOKE experiments, light sources with λ close to 770 nm were chosen to induce LSPR.

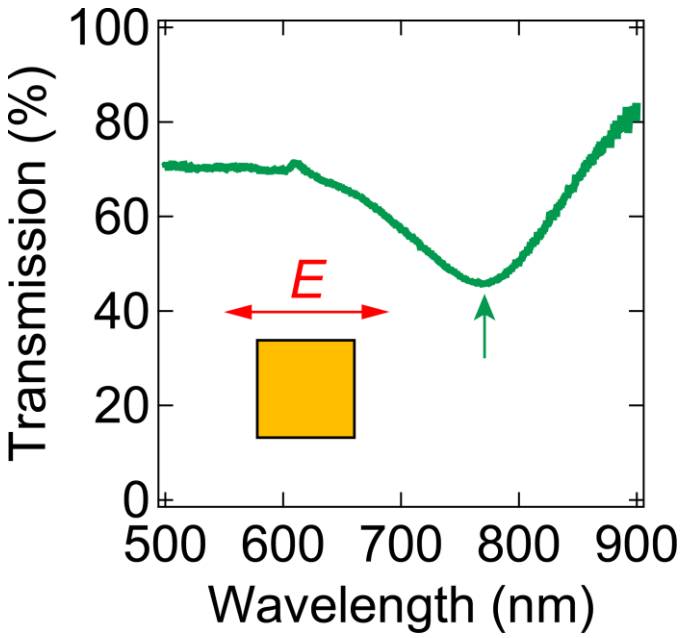

Figure 4-3. Transmission spectra of Au/Co /Au (t_{Au} = 30 nm) nanostructure.

4.4 Magnetic field dependence of L-MOKE and P-MOKE in Au/Co/Au nanostructure with different wavelength

Figure 4-4 shows the relationship between the applied magnetic field and the complex Kerr rotation in longitudinal geometry (L-MOKE curve) for Au/Co/Au (t_{Au} = 30 nm) nanostructures. Clear hysteresis loops of the L-MOKE curves were obtained for both λ = 640 nm (red circles, off-resonant condition of LSPs) and 785 nm (blue squares, on-resonant condition of LSPs). Comparing the two L-MOKE loops, there is no significant difference of the saturation field, indicated by black arrows in the figure, even by changing the wavelength of the incident light.

Figure 4-5 (a) shows the relationship between the normalized Kerr ellipticity (η) and the external magnetic field in polar geometry (P-MOKE curve) measured with λ = 500 and 750 nm in the Au/Co/Au (t_{Au} = 30 nm) nanostructures. As shown in Fig. 4-5 (a), P-MOKE curves for both λ = 500 nm (red line, off-resonant condition of LSPs) and 750 nm (blue line, on-resonant condition of LSPs) does not exhibit any hysteresis loops unlike the L-MOKE curves. Moreover, the saturated magnetization field, indicated by black arrows, in P-MOKE curves is about 10 times stronger than that of the L-MOKE curves. These results indicate that (1) Au/Co/Au nanostructure has magnetic anisotropy and (2) the easy magnetization axis is parallel to the film plane. In addition, a significant difference between the shape of the P-MOKE curves for λ = 500 and 750 nm was observed.

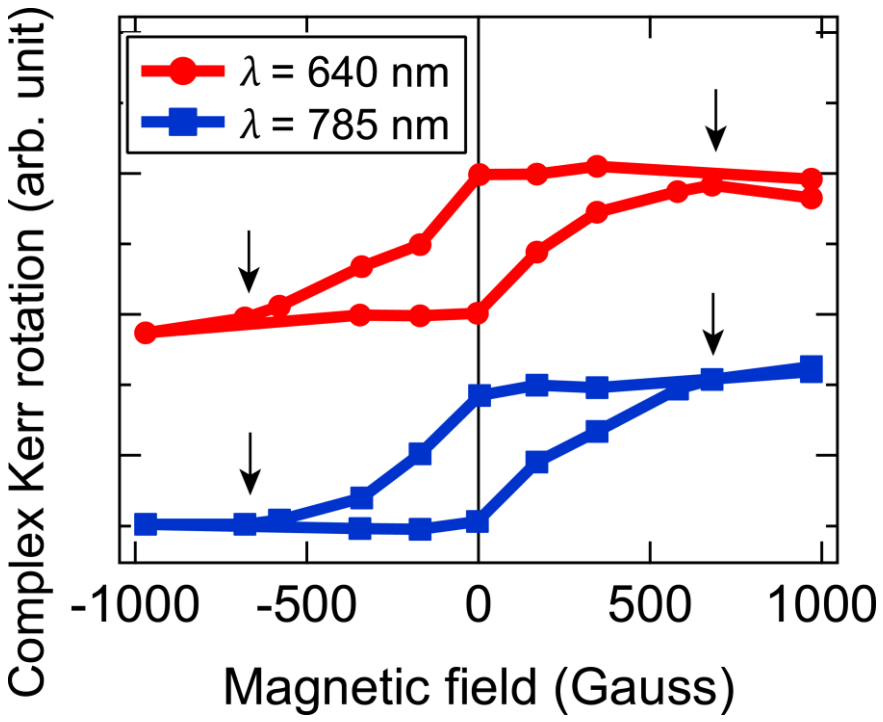

Figure 4-4. Magnetic field dependence of normalized complex Kerr rotation in longitudinal configuration (L-MOKE curve) for Au/Co/Au (t_{Au} = 30 nm) nanostructure at two different incident wavelengths (λ) : 640 nm – off-resonance (red circles and line) and 785 nm – on-resonance (blue squares and line).

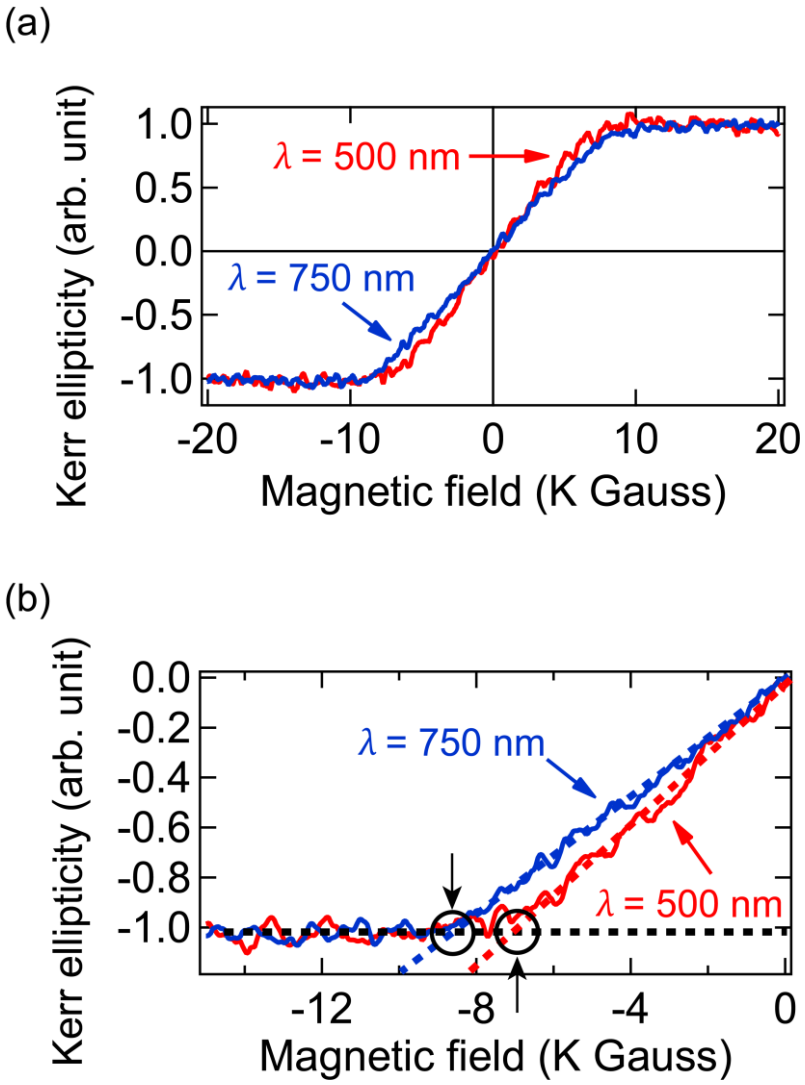

Figure 4-5. (a) Magnetic field dependence of normalized Kerr ellipticity in polar configuration (P-MOKE curve) for Au/Co/Au (t_{Au} = 30 nm) nanostructure at two different incident wavelengths (λ): 500 nm (red line) and 750 nm (blue line). (b) P-MOKE curves of Au/Co/Au nanostructure at the negative magnetic field region. Red dashed lines is the fitted data for 500 nm and blue dashed lines is for 750 nm. Black dashed line is the saturation of Kerr ellipticity. The intersection of the black dashed line and the red or the blue dashed lines gives the saturation magnetic field. Black arrows indicate the saturation magnetic fields for λ = 500 nm and 750 nm.

4.5 Estimation of magnetic anisotropy field in Au/Co/Au nanostructure

From the Fig. 4-5, a significant change of the P-MOKE curve was observed when changing the wavelength of incident light. To clarify this difference, first of all, the slope of the P-MOKE curve ($\Delta\eta$ / ΔH) was estimated in the range from -6 k to 6 k Gauss for λ = 500 and 750 nm to be 0.148 and 0.120 (unit: arb. unit of Kerr ellipticity / k Gauss), respectively. Next, the magnetic anisotropy field (H_k) in the P-MOKE curve was evaluated. H_k is defined as the intersection of the fitted line of $\Delta\eta$ / ΔH (λ = 500 nm, red dashed line; λ = 750 nm, blue dashed line) and the fitted line of the saturation Kerr ellipticity (black dashed line) in the range of -13k to -20k and 13k to 20k Gauss, shown in Fig. 4-5 (b). The average magnitude of H_k in λ = 500 and 750 nm are about 7.10k and 9.03k Gauss, respectively. From these results, it becomes clear that H_k drastically increased when the surface plasmons were excited in the structure (λ = 750 nm).

4.6 Magnetic field dependence of L-MOKE and P-MOKE in Co thin film with different wavelength

In order to investigate the wavelength dependence of H_k in a Co thin film, a 20-nm-thick Co thin film was fabricated and its H_k was measured at different wavelengths of irradiated light. Co thin film was prepared onto the ITO-coated glass substrate by electron beam evaporation. Figure 4-6 (a) shows the transmittance spectrum of the Co thin film. No absorption peak was observed in the visible to near infrared region. This means LSPs were not excited in 20-nm-thick Co thin film at the given wavelength region. Figure 4-6 (b) shows the L-MOKE curve of the Co thin film for λ = 785 nm, and it presents clear hysteresis characteristics to the applied magnetic field. Figure 4-6 (c) shows the P-MOKE curves of the Co thin film for λ = 500 nm and 750 nm. The overlapping of these two P-MOKE curves indicates that there is no wavelength dependence of H_k in the Co thin film. Therefore, I concluded that the remarkable increment of H_k in the Au/Co/Au nanostructure originated from the LSPs excited on Au.

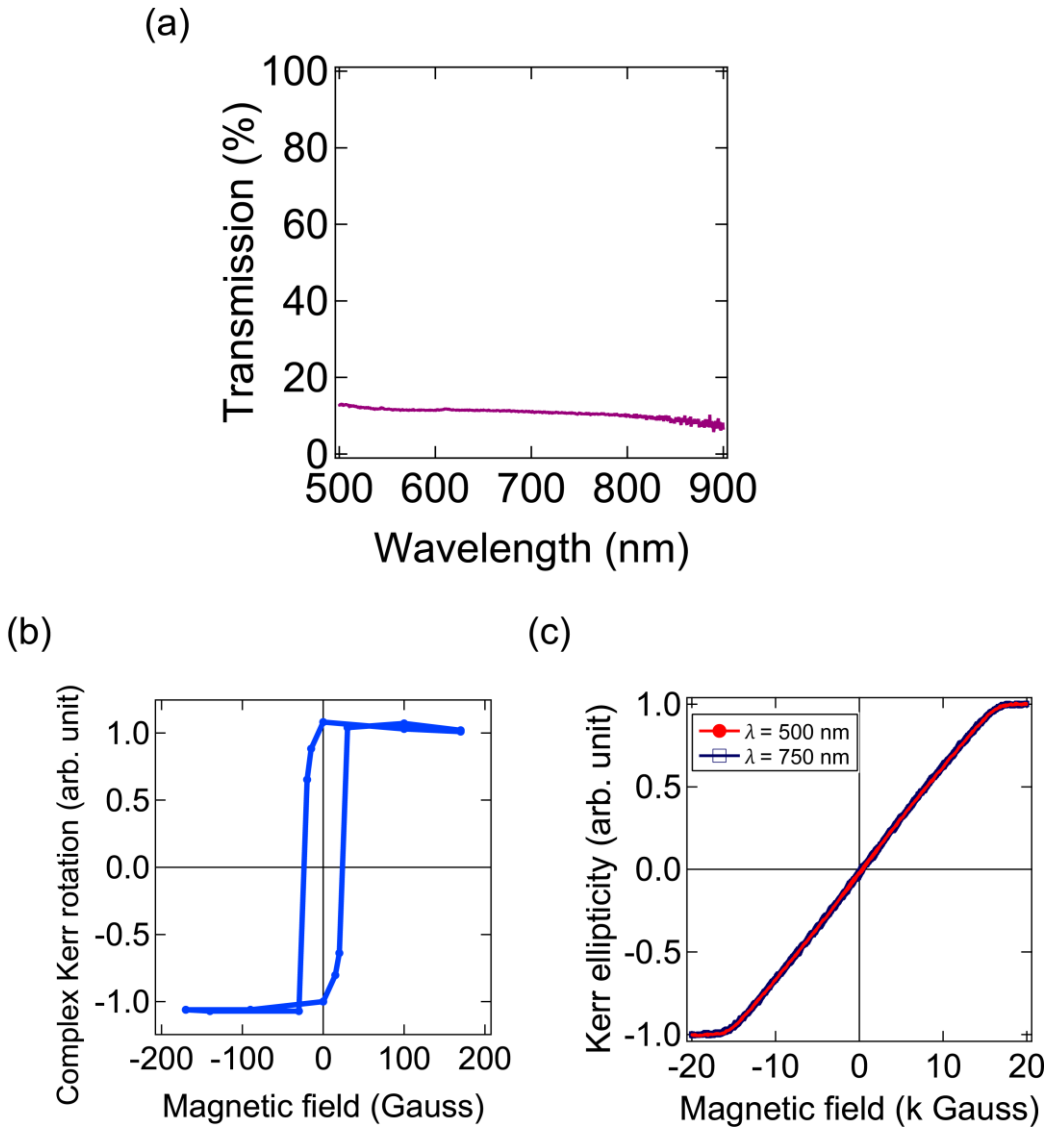

Figure 4-6. (a) Transmission spectrum of 20-nm-thick Co thin film. (b) L-MOKE curve for 20-nm-thick Co thin film. (c) P-MOKE curves for the Co thin film with two different incident wavelengths (λ): 500 nm (red circles and line) and 750 nm (blue hollow squares and line).

4.7 Calculation of in-plane magnetic anisotropy energy in Au/Co/Au nanostructure

From the magnetization curve, in-plane magnetic anisotropy energy density (K_u) in a thin film can be calculated as,

$$K_u = (\int H_\perp dM) - \left(\int H_{//} dM\right), \quad (4.1)$$

where M, $H_\perp$, and $H_{//}$ are the magnetization, magnetic field applied perpendicular and parallel to the surface of thin film, respectively. Figure 4-7 is the schematic diagram that shows the evaluation method of in-plane magnetic anisotropy from the magnetization curves. The result of dimensional analysis of magnetic anisotropy energy is shown in **APPENDIX A**. Using both L-MOKE and P-MOKE curves along with Eq. (4.1), in-plane magnetic anisotropy energy density in the Au/Co/Au nanostructure with LSPs ($K_{u,\ wLSPs}$) and without LSPs ($K_{u,\ w/oLSPs}$) were calculated, assuming a linear relationship between Kerr ellipticity (or complex Kerr rotation) and magnetization. The equations are as follows:

$$K_{u,\ wLSPs} = \frac{M_s}{\eta_s}\left(\int_0^{\eta_s} H_\perp\, d\eta_k\right)^{\lambda = 750\ nm} - \frac{M_s}{\Phi_s}\left(\int_0^{\Phi_s} H_{//}\, d\Phi_k\right)^{\lambda = 785\ nm}, \quad (4.2)$$

$$K_{u,\ w/oLSPs} = \frac{M_s}{\eta_s}\left(\int_0^{\eta_s} H_\perp\, d\eta_k\right)^{\lambda = 500\ nm} - \frac{M_s}{\Phi_s}\left(\int_0^{\Phi_s} H_{//}\, d\Phi_k\right)^{\lambda = 640\ nm}, \quad (4.3)$$

where M_s, η_s, η_k, Φ_s, and Φ_k are saturated value of magnetization, saturated Kerr ellipticity, Kerr ellipticity, saturated complex Kerr rotation, and complex Kerr rotation, respectively.

M_s = 900 emu / cm^3 was used for 6-nm-thick Co thin film based on Ref. 27. Using Eqs. (4.2) and (4.3), $K_{u,\ wLSPs}$ and $K_{u,\ w/oLSPs}$ were calculated as 0.383 × 10^6 J / m^3 and 0.310 × 10^6 J / m^3, respectively. This result indicates that in-plane magnetic anisotropy energy increases when LSPs are excited.

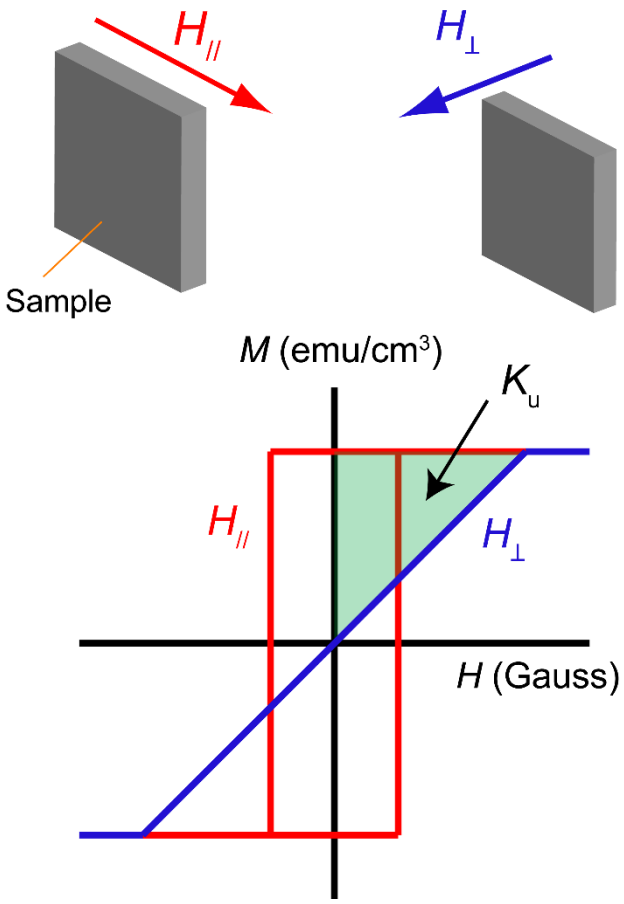

Figure 4-7. Schematic of the estimation of K_u from the magnetization (M) curves. H is the amplitude of applied magnetic field.

4.8 Au top layer thickness dependence of in-plane magnetic anisotropy energy in Au/Co/Au nanostructure

The LSP resonance induces a strong electric field near a surface of a nanostructure. The electric field is maximum at the air/metal interface, decaying drastically within the metal. In the Au/Co/Au multilayered nanostructure, the intensity of the electric field applied to the Co layer would be controlled by changing the thickness of the Au on the Co layer. In this section, first, in order to investigate the electric field distribution of square-shaped Au/Co/Au nanostructure with different Au top layer thickness, numerical calculations based on a finite element method were performed using a commercial software package (COMSOL Inc., COMSOL Multiphysics 5.3). Then, the Au top layer thickness dependence of K_u with LSPR was investigated.

Figure 4-8 (a) shows the schematic of Au/Co/Au model used for the calculations: Au bottom layer (30 nm) was set onto an SiO_2 layer with the size of 510×510×500 (height) nm^3, Co layer (6 nm) was placed onto Au bottom layer, then Au top layer with different thicknesses (t_{Au} =5, 10, 30 nm) was set on Co layer. The size of the model comprising the Au/Co/Au nanostructure is 170×170 nm. Air was selected as a substance surrounding the Au/Co/Au. The *x* and *y* directions are parallel to each edges of Au/Co/Au model, *z* direction is perpendicular to the surface of the Au/Co/Au layer, shown in Fig. 4-8 (a). A flat light source was set on the top of Au/Co/Au model that, generates the electromagnetic plane wave with polarization along the *x*-direction. Figure 4-8 (b) shows the calculation results of the transmittance spectrum of the Au/Co/Au (t_{Au} =5, 10, 30 nm) nanostructures. From these result, it was confirmed that the transmission peaks due to the LSP resonance

were appeared in the wavelength range from 700 to 800 nm in each models. Figure 4-9 (a) – (c) show the calculated electric field intensity ($|E|$) distributions of the Au/Co/Au nanostructures with various t_{Au}, (a) t_{Au} = 5 nm, (b) t_{Au} = 10 nm, and (c) t_{Au} = 30 nm, in *x*-*z* plane across the center of the Au/Co/Au nanostructure. The λ of the incident light was set to (1) the plasmon resonant wavelengths in each Au/Co/Au models introduced in Fig. 4-8 (b), and (2) 500 nm (off-LSP resonant condition). As shown in Fig. 4-9, under the LSP resonant condition, strong electric fields were generated not only at the air/Au interface but also on the surface of Co layer, while the enhancement and localization of the electric field did not appear at λ = 500 nm. Figure 4-10 shows the t_{Au} dependence of the ratio of $|E|$ in LSP resonant condition ($|E_{wLSPs}|$) and λ = 500 (off-resonant condition, ($|E_{w/oLSPs}|$) ($|E_{wLSPs}|$ / $|E_{w/oLSPs}|$) at the center of the Co surface in the Au/Co/Au nanostructures. The $|E_{wLSPs}| / |E_{w/oLSPs}|$ is greater than 1 and increases with decreasing t_{Au}. These results indicate that (1) the strong electric field is applied to the Co surface in the Au/Co/Au multilayered nanostructure by LSPR compared to the off-LSP resonant condition, and (2) the magnitude of $|E|$ applied to the Co surface in the Au/Co/Au nanostructure can be tuned by changing the t_{Au}.

Figure 4-11 (a) shows experimental results of the transmittance spectra in Au/Co/Au nanostructures with different t_{Au}. The transmission peaks were observed in the visible region. The LSP resonant wavelengths were λ = 800 nm (t_{Au} = 5 nm), 790 nm (t_{Au} = 10 nm), and 770 nm (t_{Au} = 30 nm), respectively. Moreover, the transmission peak gradually shifted to the higher wavelength region with decreasing t_{Au}. These experimental results are in good agreement with the numerical calculations.

Figure 4-11 (b) shows the t_{Au} dependence of in-plane magnetic anisotropy energy in the fabricated Au/Co/Au nanostructures with LSPs and without LSPs. $K_{u,\ wLSPs}$ is always larger than $K_{u,\ w/oLSPs}$ in the t_{Au} range of 5 to 30 nm. The ratio of $K_{u,\ wLSPs}$ to $K_{u,\ w/oLSPs}$ ($K_{u,\ wLSPs}$ / $K_{u,\ w/oLSPs}$) with respect to t_{Au} is shown in Fig. 4-11 (c). Considering the measurement error, the estimated $K_{u,\ wLSPs}$ / $K_{u,\ w/oLSPs}$ shows an almost constant value regardless of t_{Au}. These results imply that K_u increase by the LSPR in Au/Co/Au nanostructures occurs, even though the Au top layer on Co layer becomes thick, while the increase ratio of K_u by LSP resonance is insensitive to the change of Au top layer thickness.

At this stage, it is difficult to claim whether the electric field induced by LSPR affects K_u in Au/Co/Au nanostructure or not, but I can give plausible explanation of the results. One possibility is that the variation of the applied electric field intensity in the Co layer when changing the t_{Au}, which is estimated to be 32 %, is not sufficient to make a difference in $K_{u,}$ based on the assumption that K_u enhancement is attributed to the electric field increase in the Co layer. Another possibility is that the electric field induced by the LSPR does not particularly contribute to the enhancement of K_u. If this is the case, it is necessary to discuss the plasmon resonance-induced K_u enhancement from a different view-point such as light absorption.

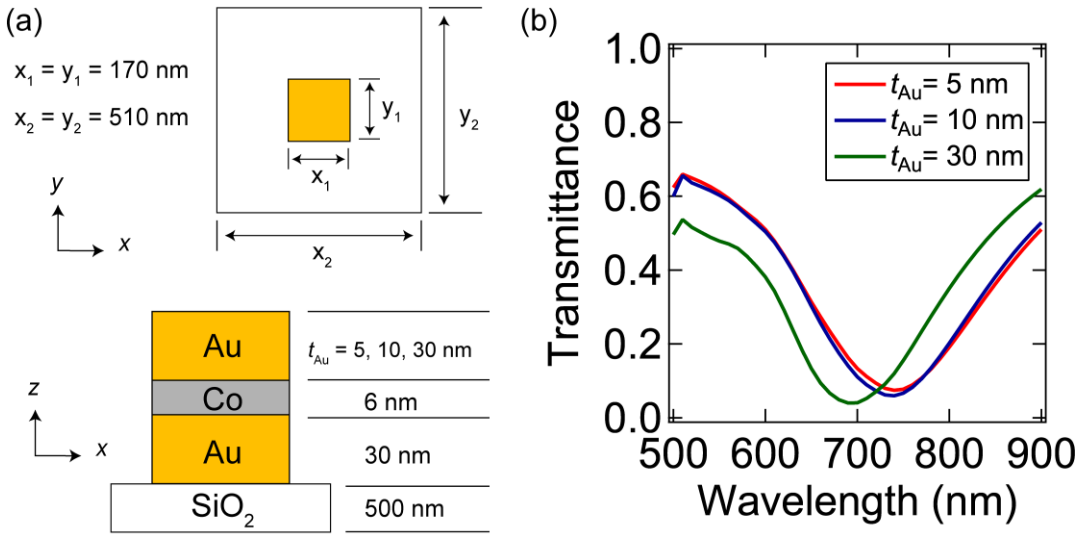

Figure 4-8. (a) Au/Co/Au model with different Au top layer thickness (t_{Au}) used for the numerical calculation based on a finite element method. (b) Simulated transmittance spectrum of Au/Co/Au (t_{Au} = 5, 10, 30 nm) model.

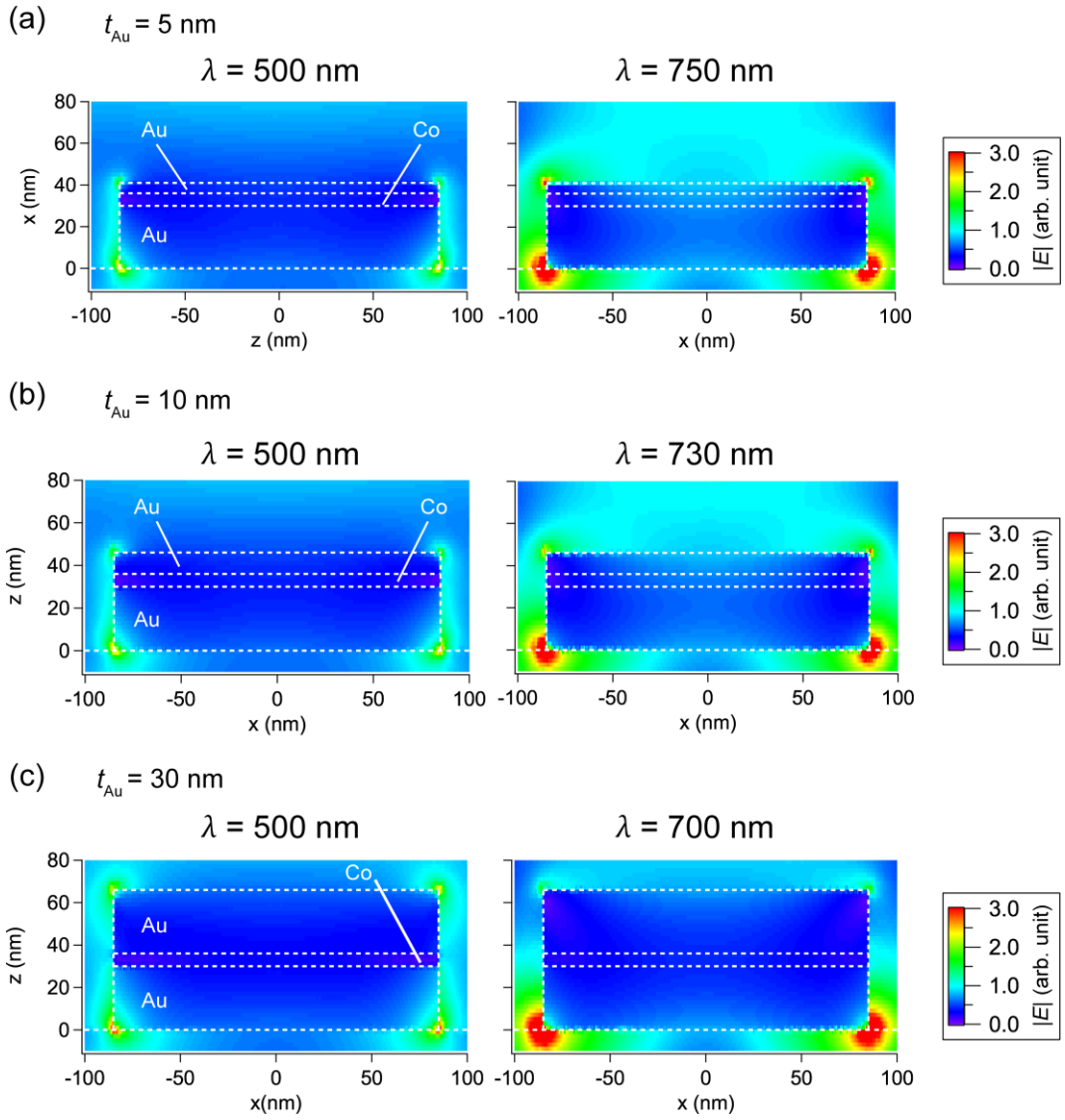

Figure 4-9. Simulated distributions of the electric field intensity (|*E*|) in the Au/Co/Au models with different t_{Au} = (a) 5 nm, (b) 10 nm, and (c) 30 nm in the *x*-*z* plane across the center of the Au/Co/Au models at the wavelength (λ) of 500 nm and the LSP resonant wavelengths (750, 730, and 700 nm).

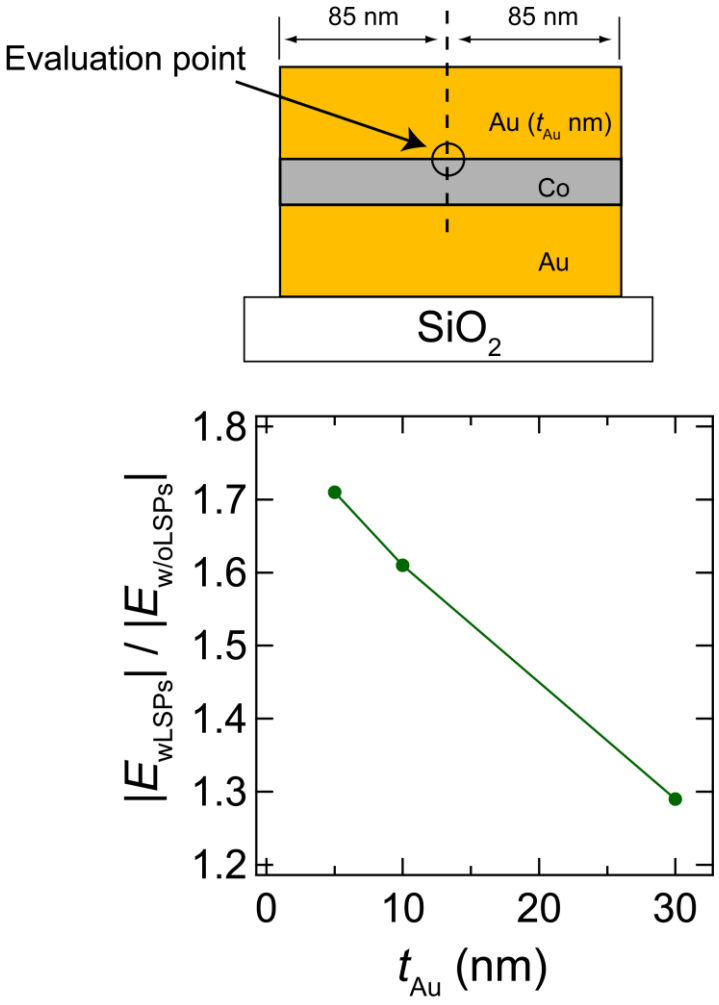

Figure 4-10. The ratio of the electric field intensity ($|E|$) in LSP resonant condition ($|E_{wLSPs}|$) and λ = 500 (off-resonant condition, $|E_{w/oLSPs}|$) ($|E_{wLSPs}| / |E_{w/oLSPs}|$) at the center of the Co surface in the Au/Co/Au models with different Au top layer thickness (t_{Au}) as a function of t_{Au}.

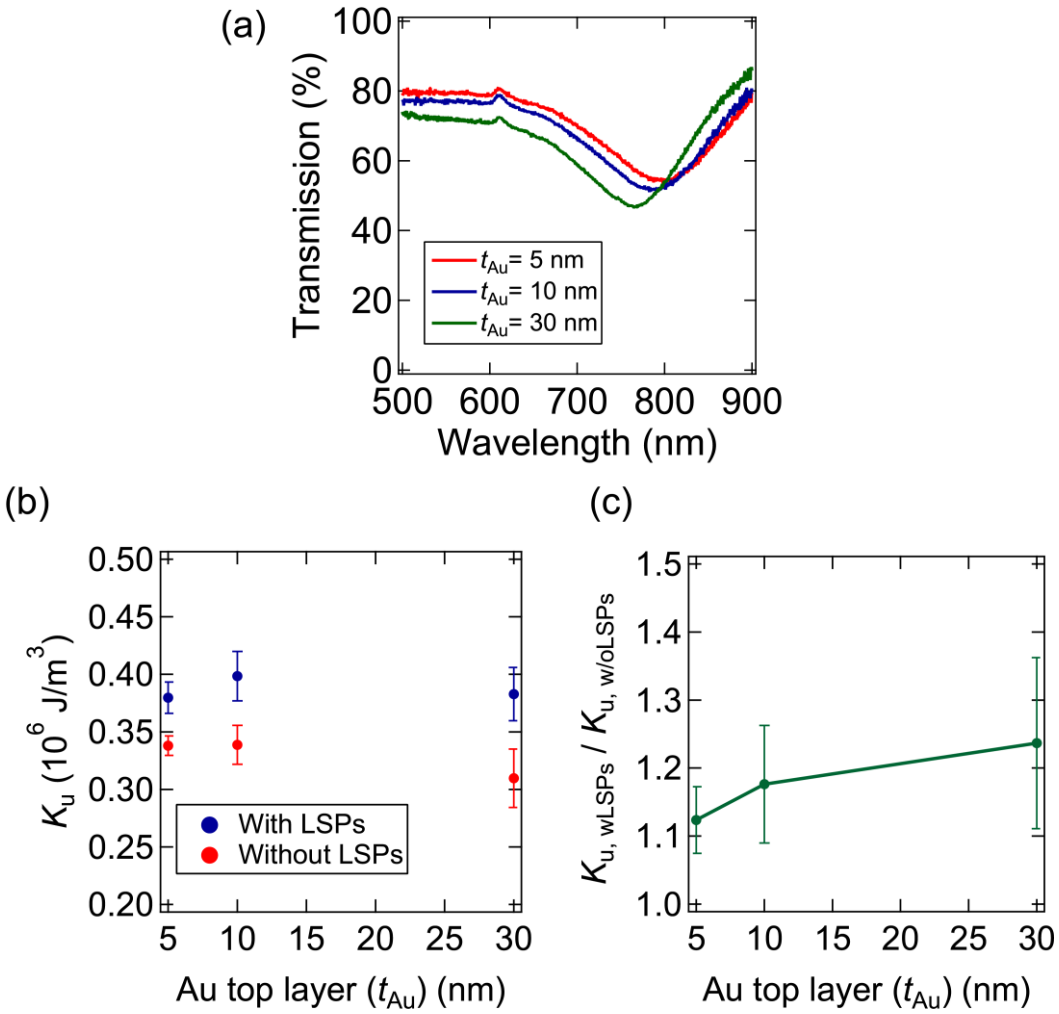

Figure 4-11. (a) Experimental results of transmission spectrum in Au/Co/Au (t_{Au} = 5, 10, and 30 nm) nanostructures. (b) The t_{Au} dependence of K_u with or without LSP resonance. (c) The ratio of K_u at the LSP resonant condition ($K_{u, wLSPs}$) and off-resonant condition ($K_{u, w/oLSPs}$) ($K_{u, wLSPs}$ / $K_{u, w/oLSPs}$) with respect to the t_{Au}.

4.9 Consideration of the mechanism in plasmon resonance induced in-plane magnetic anisotropy energy increase

In a thin film, magnetic anisotropy energy consists of both magnetocrystalline anisotropy energy and shape anisotropy energy [4.28, 4.29]. In this work, the magnetic anisotropy energy modulation would come from the change of magnetocrystalline anisotropy energy because the same sample was used in all experiments and no sample deformation was verified through all experiments.

To understand the results, let me discuss about the thermal effect on magnetic anisotropy energy due to temperature increase from plasmon induced light absorption [4.30]. There are many theoretical and experimental works on the temperature dependence of magnetocrystalline anisotropy energy [4.31 – 4.33]. In all these works, a decrease in the magnetocrystalline anisotropy energy has been observed with an increase of temperature. My results, on the other hand, are different from these, because in-plane magnetic anisotropy energy increases as temperature increases. To explain these results, some possible scenarios are presented.

As stated above, total in-plane magnetic anisotropy energy K_u, which can be estimated from the magnetization loops shown in Fig. 4-5 and Fig. 4-6 (c), is written as a sum of shape anisotropy energy K_s, which comes from magnetostatic property, and magnetocrystalline anisotropy energy K_i, which is contributed from the crystal structure in a substance, as below,

$$K_u = K_s + K_i. \quad (4.4)$$

In the case of a thin film structure, whose lateral dimensions are treated as infinitely long compared to its thickness, the magnetization direction tends to align along the in-plane direction due to shape anisotropy and K_s has a positive value. As shown in **APPENDIX B**, which shows the experimental result of K_u in Au/Co/Au thin film, the value of K_s can be calculated in a thin film. However, when the size of the structure is at the nanometer scale, the estimation and calculation of K_s is difficult and unreliable, because (1) the magnetization distribution in the square-shaped nanostructure is complicated [4.34] and (2) the magnetization of the magnetic nanostructure cannot be measured directly. From the calculation result of magnetostatic energy found in Ref. 4.34, the magnetization vector is easily aligned to the in-plane direction compared to out-of-plane in the square nanostructure and, at this point, what I can say is K_s in Au/Co/Au nanostructure has a positive sign but its value is still unknown. Meanwhile, for K_i, its value can be calculated by subtracting K_s from K_u in the case of a thin film with infinitely long lateral dimensions. However, in a nanostructure that has finite dimensions, the value of K_i cannot be obtained by calculation because reliable calculation of K_s cannot be performed. Hence, it is possible to build up two hypotheses. One is K_i has a negative value and another is that it has a positive value.

Assuming that the sign of K_i is negative, which means the magnetization of nanostructure is perpendicular to the film surface, K_i reduces K_u and K_s should be larger than $|K_i|$ because K_u was positive which has already been confirmed above using the L-MOKE and P-MOKE loops. Under this condition, as shown in Fig. 4-12, when the

temperature of the structure increases due to the plasmon resonance, K_i that is negative approaches zero, and as a result, K_u increases effectively. A similar phenomenon has been observed and reported in magnetic thin film, which has characteristics of reorientation phase transition, but never in nanostructures [4.35].

Another possibility is the sign of K_i is positive, which is same to that of Au/Co/Au thin film shown in **APPENDIX B**. As shown in Fig. 4-13 (a), when K_i has a positive value and decreases with the temperature increase by LSP excitation, K_u also always decreases. In this case, to explain my results showing an overall K_u increase by LSP resonance plausibly, it is necessary to introduce a new term K_p, which is the plasmon-induced in-plane magnetic anisotropy energy (Fig. 4-13 (b)). Moreover, even if the K_i decreases with increasing temperature by LSP excitation, K_p increases K_u more than the decrease of K_i. Finally, I propose a possible origin of plasmon-induced in-plane magnetic anisotropy. As described in **Chapter 1**, when LSPs are resonantly excited by light in metal nanostructure, collective electron oscillations are induced by the electric field of the incident light. In other words, electric polarization is induced in the metal nanostructure by LSP excitation. According to Ref. 4.36, by using a ferromagnetic insulator, they derived an expression to describe the electric polarization, $\vec{P}$, dependence of magnetocrystalline anisotropy energy (K_i), which is,

$$K_i' = K_i + \left(\frac{\partial K_i'}{\partial \vec{P}}\right)_0 \cdot \vec{P}, \tag{4.5}$$

where K_i' is the $\vec{P}$-dependent K_i. Therefore, magnetocrystalline anisotropy energy increase via LSP resonance-induced electric polarization may be essential for the overall

K_u increase by LSP resonance. If this is the case, K_p increases as a function of the incident light intensity because the electric polarization is proportional to the applied electric field.

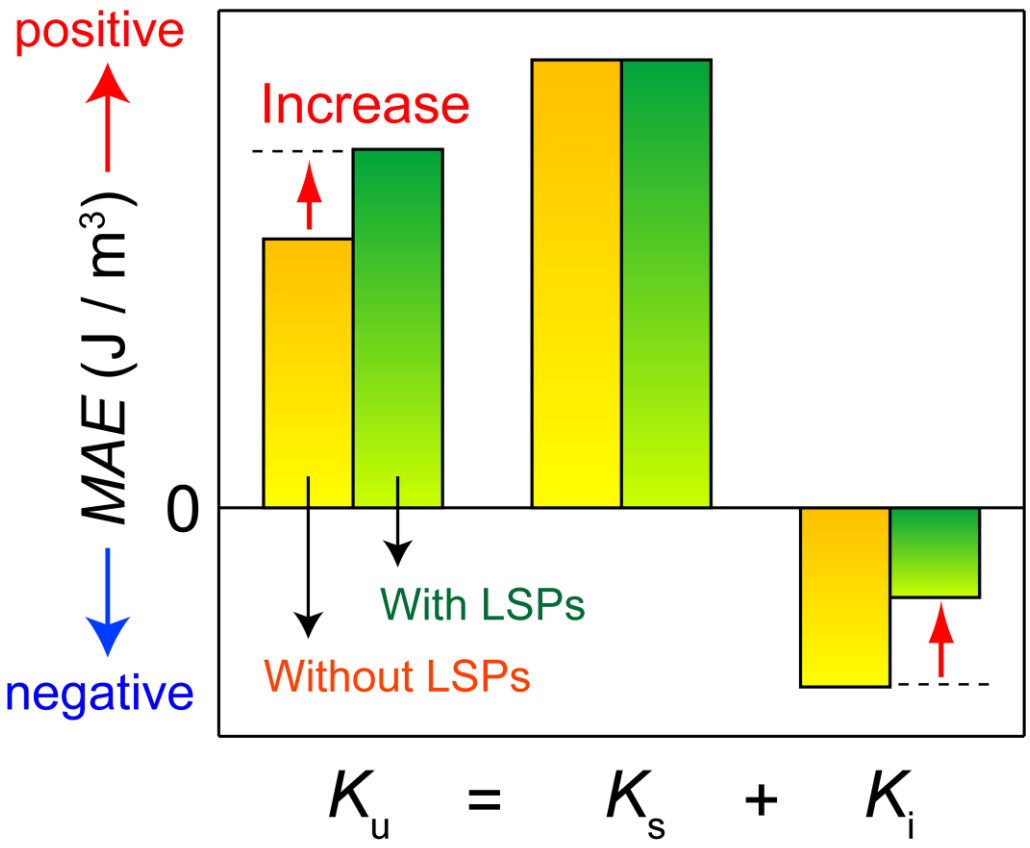

Figure 4-12. Illustration of K_u increase by LSPs in Au/Co/Au nanostructure. The sign of K_i is assumed to be negative.

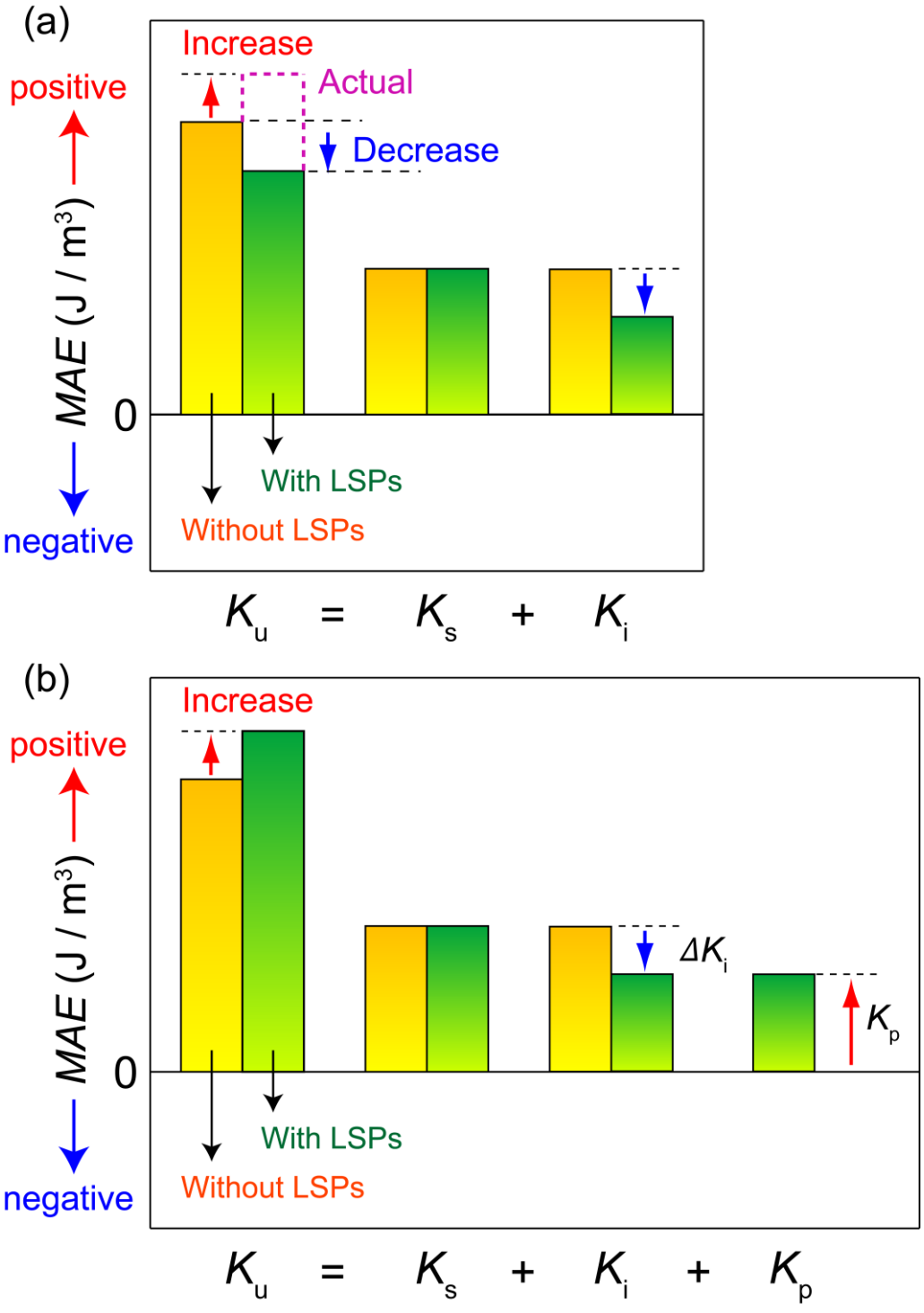

Figure 4-13. Illustrations of K_u modification by LSPs in Au/Co/Au nanostructure (a) without K_p, and (b) with K_p. The sign of K_i is assumed to be positive.

4.10 References

4.1. **Y. Kikuchi**, and T. Tanaka, Scientific Reports, submitted (2018).

4.2. Y. Onose, N. Takeshita, C. Terakura, H. Takagi, and Y. Tokura, Physical Review B **72**, 224431 (2005).

4.3. M. Matsushita, S. Endo, K. Miura, and F. Ono, Journal of Magnetism and Magnetic Materials **269**, 393 (2004).

4.4. T. Iwamoto, M. Mito, M. Hidaka, T. Kawase, and K. Takeda, Physica B **329**, 667 (2003).

4.5. P-J. Hsu, A. Kubetzka, A. Finco, N. Romming, K. V. Bergmann, and R. Wiesendanger, Nature Nanotechnology **12**, 123 (2017).

4.6. **Y. Kikuchi**, T. Seki, M. Kohda, J. Nitta, and K. Takanashi, Journal of Physics D-Applied Physics **46**, 285002 (2013).

4.7. T. Maruyama, Y. Shiota, T. Nozaki, K. Ohta, N. Toda, M. Mizuguchi, A. A. Tulapurkar, T. Shinjo, M. Shiraishi, S. Mizukami, Y. Ando, and Y. Suzuki, Nature nanotechnology **4**, 158 (2009).

4.8. S. Ohkoshi, K. Imoto, Y. Tsunobuchi, S. Takano, and H. Tokoro, Nature chemistry **3**, 564 (2011).

4.9. T. V. Brinzari, D. Rajan, C. F. Ferreira, S. A. Stoian, P. A. Quintero, M. W. Meisel, and D. R. Talham, Journal of Applied Physics **124**, 103904 (2018).

4.10. D. Pinkowicz, M. Rams, M. Mišek, K. V. Kamenev, H. Tomkowiak, A. Katrusiak, and B. Sieklucka, Journal of the American chemical society **137**, 8795 (2015).

4.11. A. V. Kimel, A. Kirilyuk, and T. Rasing, Laser & Photonics Reviews **1**, 275 (2007).

4.12. S. Mangin, M. Gottwald, C-H. Lambert, D. Steil, V. Uhlír, L. Pang, M. Hehn, S. Alebrand, M. Cinchetti, G. Malinowski, Y. Fainman, M. Aeschlimann, and E. E. Fullerton, Nature materials **13**, 286 (2014).

4.13. C-H. Lambert, S. Mangin, B. S. D. Ch. S. Varaprasad, Y. K. Takahashi, M. Hehn, M. Cinchetti, G. Malinowski, K. Hono, Y. Fainman, M. Aeschlimann, and E. E. Fullerton, Science **345**, 1337 (2014).

4.14. D. Meneses-Rodriguez, E. Ferreiro-Vila, P. Prieto, J. Anguita, M. U. Gonzalez, J. M. Garcia-Martin, A. Cebollada, A. Garcia-Martin, and G. Armelles, Small **7**, 3317 (2011).

4.15. N. Maccaferri, A. Berger, S. Bonetti, V. Bonanni, M. Kataja, Q. H. Qin, S. van Dijken, Z. Pirzadeh, A. Dmitriev, J. Nogues, J. Akerman, and P. Vavassori, Physical Review Letters **111**, 167401 (2013).

4.16. H. Yamane, K. Takeda, and M. Kobayashi, Applied Physics Letters **106**, 052409 (2015).

4.17. C. A. Herreňo-Fierro, E. J. Patiňo, G. Armelles, and A. Cebollada, Applied Physics Letters **108**, 021109 (2016).

4.18. B. C. Choi, H. Xu, G. Hajisalem, and R. Gordon, Applied Physics Letters **112**, 022403 (2018).

4.19. G. Armelles, A. Cebollada, A. Garcia-Martin, and M. U. Gonzalez, Advanced Optical Materials **1**, 10 (2013).

4.20. D. Sander, S. O. Valenzuela, D. Makarov, C. H. Marrows, E. E. Fullerton, P. Fischer, J. McCord, P. Vavassori, S. Mangin, P. Pirro, B. Hillebrands, A. D. Kent, T. Jungwirth, O. Gutfleisch, C. G. Kim, and A. Berger, Journal of Physics D-Applied Physics **50**, 33 (2017).

4.21. **Y. Kikuchi**, and T. Tanaka, Japanese Journal of Applied Physics Rapid Communication **57**, 110305 (2018).

4.22. X. W. Wu, K. Y. Guslienko, R. W. Chantrell, and D. Weller, Applied Physics Letters **82**, 3475 (2003).

4.23. G. Kim, Y. Sakuraba, M. Oogane, Y. Ando, and T. Miyazaki, Applied Physics Letters **92**, 172502 (2008).

4.24. W. A. Challener, T. W. Mcdaniel, C. D. Mihalcea, K. R. Mountfield, K. Pelhos, and I. Sendur, Japanese Journal of Applied Physics **42**, 981 (2003).

4.25. F. Zavaliche, T. Zhao, H. Zheng, F. Straub, M. P. Cruz, P. L. Yang, D. Hao, and R. Ramesh, Nano Letters **7**, 1586 (2007).

4.26. K. Sato, H. Hongu, H. Ikekame, Y. Tosaka, M. Watanabe, K. Takanashi, and H. Fujimori, Japanese Journal of Applied Physics Part 1-Regular Papers Short Notes & Review Papers **32**, 989 (1993).

4.27. T. C. Chuang, P. L. Su, P. H. Wu, and S. Y. Huang, Physical Review B **96**, 174406 (2017).

4.28. D. Weller, J. Stohr, R. Nakajima, A. Carl, M. G. Samant, C. Chappert, R. Megy, P. Beauvillain, P. Veillet, and G. A. Held, Physical Review Letters **75**, 3752 (1995).

4.29. T. Kojima, M. Mizuguchi, T. Koganezawa, K. Osaka, M. Kotsugi, and K. Takanashi, Japanese Journal of Applied Physics **51**, 010204 (2012).

4.30. G. Baffou, R. Quidant, and C. Girard, Applied Physics Letters **94**, 153109 (2009).

4.31. C. Zener, Physical Review **96**, 1335 (1954).

4.32. Y. Melikhov, J. E. Snyder, D. C. Jiles, A. P. Ring, J. A. Paulsen, C. C. H. Lo, and K. W. Dennis, Journal of Applied Physics **99**, 08r102 (2006).

4.33. S. Yoon, and K. M. Krishnan, Journal of Applied Physics **109**, 07b534 (2011).

4.34. R. P. Cowburn, and M. E. Welland, Applied Physics Letters **72**, 2041 (1998).

4.35. A. Berger, and H. Hopster, Journal of Applied Physics **79**, 5619 (1996).

4.36. G. T. Rado, and J. M. Ferrari, Physical Review B **12**, 5166 (1975).

Chapter 5

Summary

This thesis presents a study of the interaction between the localized surface plasmon excitation and the magnetic properties focusing the magneto-optical Kerr effect and magnetic anisotropy energy. The research of the magneto-plasmonics, a field that merges the concepts from plasmonics and magnetics, has started just one decade ago from the observation of the large magneto-optical effect at the resonant wavelength of surface plasmons. However, there remain suspicion that magneto-optical effect enhancement really comes from the surface plasmon excitation. Moreover, magneto-plasmonics is still in its infancy and there is still much unexplored physics to be discussed. This work's significance is showing the clear evidence of the plasmon excitation-induced magnetic properties modification. First, this work provides a clear evidence that magneto-optical Kerr effect is enhanced by the localized surface plasmon excitation, and demonstrates that plasmon excitation is effective to improve the performance of magneto-optical device. Second, this work gives the first demonstration of surface plasmon modification of the magnetic anisotropy energy in magnetic material. Through the consideration of the possible mechanism, the presence of plasmon-induced magnetocrystalline anisotropy is suggested.

The knowledge obtained from this work would contribute to the development of a real application such as magnetically controlled optical isolator, modulator beyond the current limitation. In addition, the new concept such as plasmonic control of magnetic anisotropy,

which is provided in this work, encourages studies on advanced magneto-plasmonic phenomena and applications for magnetic devices. Plasmonic modification of the magnetic property in a material has a potentially high impact not only in material science but also in other research fields such as nanophotonics, plasmonics, magnetics and spintronics.

In **Chapter 1**, the background knowledges of plasmonics and magneto-optics were presented to promote the understanding of contents in this thesis. Then a review of the current research on magneto-plasmonics was introduced. Finally, the scope of this research was defined.

Chapter 2 presented the theoretical framework and experimental results of magneto-optical Kerr effect, which is main tool for evaluating the magnetic properties in this work. This chapter begins with the explanation of the origin of the magneto-optical effects from the macroscopic view. The discussion moves to how to experimentally evaluate the magneto-optical Kerr effect. The evaluation principle of (1) Kerr rotation, and (2) Kerr ellipticity by the usage of photoelastic modulator and the linear polarizer, was theoretically and mathematically introduced. Based on these knowledge, longitudinal magneto-optical Kerr effect (L-MOKE) measurement system was constructed in this work. Next, theoretical analysis of the L-MOKE activity in Co thin film with different polarized light was carried out. Comparing the experimental results, it was shown that the difference of L-MOKE activity in Co thin film by changing the polarization direction is below 7 % at the incident angle of 14 degrees. The shaped-induced L-MOKE activity anisotropy was also discussed. In the rectangular-shaped Co nanostructures without

plasmon resonance, the L-MOKE activity is almost stable even though the polarization direction of incident light is changed. This makes it possible to conclude that the shape-induced L-MOKE enhancement can be ignored in the fabricated Co nanostructure. These knowledge were succeeded to the design of Au/Co/Au nanostructures, fabricated in **Chapter 3**.

In **Chapter 3**, the work for the relationship between the L-MOKE activity enhancement and the localized surface plasmon (LSP) excitation is summarized. This chapter starts the brief introduction of background and motivation in this work. Then, the fabrication procedure of rectangular-shaped Au/Co/Au nanostructures was demonstrated. From the transmission spectrum results of Au/Co/Au nanostructures, the wavelength of the LSP resonance can be tuned by changing the short axis length of rectangular structure. Moreover, the LSP excitation on or off can be switched by changing the polarization direction of incident light at the wavelength of 785 nm. From the evaluation of L-MOKE activity by changing the polarization direction in Au/Co/Au rectangular nanostructures with systematically varied short axis length, the largest L-MOKE activity was observed under the LSP excitation, concluding that it has a clearly relationship between the strong enhancement of L-MOKE activity and the LSP excitation. For the next step, the magneto-optical figure of merit (FOM), which reflects the signal-to-noise ratio of MO signal in magneto-optical devices, was also evaluated to discuss the effectiveness of plasmon excitation for the performance of magneto-optical devices. The resulting that the LSP excitation contributes to improve the FOM due to the increase of not only Kerr rotation but also the reflectivity in Au/Co/Au nanostructure. Moreover, the FOM in Au/Co/Au nanostructure with LSP excitation and bare Co nanostructure was compared, resulting

that the addition of plasmonic Au layer to Co layer plays an important role for improve not only MO activity but also FOM.

Chapter 4 presents the work for the modification of in-plane magnetic anisotropy energy (K_u) in Au/Co/Au nanostructure by LSP resonance. This chapter begins with the introduction of background in magnetization control technique and the motivation of this work. Then, the evaluation method of magnetization curves in square-shaped Au/Co/Au nanostructures through the L-MOKE and polar magneto-optical Kerr effect (P-MOKE) measurements was explained. From the transmittance spectra results, the LSP resonant wavelength of Au/Co/Au nanostructure was observed at 770 nm, and no other absorption peaks were not observed. Therefore, LSP excitation can be switched by changing the wavelength of incident light. In the next stage, L-MOKE curves and P-MOKE curves in Au/Co/Au nanostructure were evaluated for both LSP resonant wavelength and off-resonant wavelength. Comparing the saturation fields of P-MOKE and L-MOKE curves, Au/Co/Au nanostructure has a magnetic anisotropy and the easy magnetization axis is parallel to the film plane. In L-MOKE curves, there is no significant change of saturation field even though the wavelength of incident light was changed. However, the significant increase of saturation field was shown in P-MOKE curves when LSP resonance was excited. Through the estimation of K_u from the P-MOKE and L-MOKE curves, K_u increased because of LSP resonance. Through the discussion of the possible mechanism of K_u increase by LSP resonance from the perspective of the thermal effect on the magnetic anisotropy, I concluded that the magnetocrystalline anisotropy modification would play a key role to increase an effective in-plane magnetic anisotropy energy increase by LSP resonance.

List of Publications

List of Papers:

1. **Y. Kikuchi**, and T. Tanaka, "Strengthen of magnetic anisotropy of Au/Co/Au nanostructure by surface plasmon resonance", Scientific Reports, submitted (2018).

2. **Y. Kikuchi**, and T. Tanaka, "Plasmon assisted improvement of figure of merit of magneto-optical Kerr effect in Au/Co/Au multilayered nanorectangular patch array", Japanese Journal of Applied Physics Rapid Communication **57**, 110305 (2018).

3. **Y. Kikuchi**, T. Seki, M. Kohda, J. Nitta, and K. Takanashi, "Voltage-Induced Coercivity Change in FePt/MgO stacks with different FePt thicknesses", Journal of Physics D-Applied Physics **46**, 285002 (2013).

4. T. Seki, **Y. Kikuchi**, and K. Takanashi, "Interface magnetic anisotropy between L10-FePt and Nonmagnetic layers", IEEE Transactions on Magnetics **48**, 3199 (2012).

List of Presentations (International Conference):

1. **Y. Kikuchi**, and T. Tanaka,
   "Increase of magnetic anisotropy energy in Au/Co/Au nanostructure by localized surface plasmon resonance",
   JSAP-OSA Joint Symposia 2018, (Nagoya Congress Center, Nagoya, Aichi, Japan), Sep. 18, **2018**. (ORAL)

2. **Y. Kikuchi**, and T. Tanaka,
   "Magneto-optical Kerr effect enhancement by localized plasmon resonance in Au/Co/Au nanostructure",
   The 7th Advanced Lasers and Photon Sources (ALPS2018), (Pacifico Yokohama, Yokohama, Kanagawa, Japan), April 25, **2018**. (ORAL)

3. **Y. Kikuchi**, and T. Tanaka,
   "Localized plasmon resonance enhanced magneto – optical Kerr effect",
   The 2nd International Symposium on Optically-assisted Mechanical Systems & the 2nd RIKEN-nCOMS Joint Symposium, (Yonsei University, Seoul, Korea), Dec. 18, **2017**. (ORAL, Invited)

4. **Y. Kikuchi**, T. Seki, M. Kohda, J. Nitta, and K. Takanashi,
   "Coercivity change by applying voltage in L10-FePt / MgO stacks",
   Summit of Materials Science (SMS2012), (Tohoku University, Sendai, Miyagi, Japan), Nov. **2012**. (Poster)

5. **Y. Kikuchi**, T. Seki, M. Kohda, J. Nitta, and K. Takanashi,
   "Voltage-induced coercivity change in Au / L10-FePt / MgO stacks with interface magnetic anisotropy",
   The 21th International Colloquium on Magnetic Films and Surfaces (ICMFS2012), (Shanghai, China), Sep. **2012**. (Poster)

6. **Y. Kikuchi**, T. Seki, and K. Takanashi,
   "Interfacial Magnetic Anisotropy between L10- FePt and Nonmagnetic Layers",
   International Magnetics Conference (INTERMAG 2012), (Vancouver, Canada), May **2012**. (Poster)

List of Presentations (Domestic Conference):

1. **Y. Kikuchi**, and T. Tanaka,
   "Magneto-optical property in Au/Co/Au rectangular nano rod",
   The 65th JSAP Spring Meeting, 2018, (Waseda University, Tokyo, Japan), March 17, **2018**. (ORAL)

2. **Y. Kikuchi**, and T. Tanaka,
   "Magneto-optical properties of Au/Co/Au stacked film introducing plasmonic structure",
   The 78th JSAP Autumn Meeting, 2017, (Fukuoka Convention Center, Fukuoka, Japan), Sep. 8, **2017**, (ORAL)

3. **Y. Kikuchi**, T. Seki, M. Kohda, J. Nitta, and K. Takanashi,
   "Electric field control of coercivity in L10-FePt / MgO stacks with interface magnetic anisotropy",
   The 73th JSAP Autumn Meeting, 2012, (Matsuyama, Ehime, Japan), Sep. **2012**, (ORAL)

4. **Y. Kikuchi**, T. Seki, and K. Takanashi,
   "Effect of capping layers on perpendicular magnetic anisotropy of FePt thin films"
   The 59th JSAP Spring Meeting, 2012, (Tokyo, Japan), March **2012**. (Poster)

Awards:

1. Graduation with top honors from department of material science at Nagoya Institute of Technology, March **2011**.

Funding:

1. RIKEN Junior Research Associate (JRA) program from FY2017 to FY2018.

Acknowledgements

I would first like to express my gratitude to my Academic Supervisor, Specially Appointed Professor Takuo Tanaka, for giving me the opportunity to pursue my doctoral studies here in Tokyo Institute of Technology. Without his belief in my ability and my desire to do research, all this would not be possible. I also thank him to give the opportunity to do research in RIKEN as a member of Metamaterials Laboratory. The research experience in RIKEN has taught me a lot of important things to carry out a frontier research.

I would like to thank to Professor Masahiko Hara, Professor Akira Ohtomo, Professor Taro Hitosugi, Associate Professor Hiroyuki Wada, and Associate Professor Takumi Sannomiya, for their questions during my defense, which have helped me gain an even deeper understanding of my own work. Their insightful comments and suggestion have helped further improve the structure and content of my doctoral thesis.

I would like to thank Dr. Gen Tatara, Team leader of Spin Physics Theory Research Team in RIKEN, for his valuable comments from the perspective of a theory for spin physics.

I appreciate Dr. Jorge Luis Puebla Nunez, Postdoctoral Researcher of Quantum Nano-Scale Magnetism Team in RIKEN, for giving the helpful advice of longitudinal magneto-optical Kerr effect measurement system construction.

I would like to thank Dr. Haruki Yamane, Researcher in Akita Industrial Technology Center, for the usage of polar magneto-optical Kerr effect measurement system.

I would like to thank all of Tanaka group members, Dr. Thu Hac Huong Le, Dr. Bikas Ranjan, Ms. Olaya Cherrie May Mogueis, Mr. Dong-Sheng Su, Mr. Yuki Sakamoto, Dr. Renilkumar Mudachathi, Dr. Yukie Yokota, Dr. Yuto Moritake, and Dr. Thanh Tung Nguyen, for their useful comments in a regular science meeting. Especially, I sincerely acknowledge my colleague Dr. Maria Vanessa Balois for her English correction, useful comments, and her kindness through the lab life. I thank to secretary in Tanaka Group, Ms. Yi-Jung Liang, for helping business routine. I acknowledge technical staff Ms. Keiko Awano for lecturing a lot of facilities operation. I thank to my juniors in lab, Mr. Yuta Shimoda, Mr. Ryuto Tateyama, Mr. Yuki Nakamura, Mr. Ryutaro Ikeda, and Ms. Taeko Matsukata, an undergraduate student in Gakushuin University, for making a great atmosphere in our living room. Through the teaching experience for them, I have learned the difficulty to direction of junior, and have felt the delight to see the growth of them.

I would like to thank RIKEN's program for Junior Scientists and for the financial support provided to me as a Junior Research Associate.

Finally, I appreciate my parents and my elder sister for keeping encourage me in Ph. D. student life.

Feb. 2019

Yusuke Kikuchi

APPENDIX A

Dimensional analysis of magnetic anisotropy energy

In **Chapter 4**, in-plane magnetic anisotropy energy (K_u) was calculated from the P-MOKE and L-MOKE loops, assuming a linear relationship between Kerr ellipticity (or complex Kerr rotation) and magnetization. Generally, K_u can be estimated from the area enclosed by the two magnetization curves, in which magnetic field is applied parallel or perpendicular to the surface plane of sample, in magnetization curve. Here, a dimensional analysis of K_u is introduced.

Generally, the unit of magnetization in a material and magnetic field applied to sample are described as emu/cm^3, and Gauss. Therefore, the unit of K_u is,

$$K_u = \text{emu} \times \text{cm}^{-3} \times \text{Gauss}. \tag{A.1}$$

Then, Gauss and emu can be converted as,

$$\text{Gauss} = \text{g}^{\frac{1}{2}} \times \text{cm}^{-\frac{1}{2}} \times \text{s}^{-1}, \tag{A.2}$$

$$\text{emu} = \text{g}^{\frac{1}{2}} \times \text{cm}^{\frac{5}{2}} \times \text{s}^{-1}. \tag{A.3}$$

By applying Eq. (A.2) and (A.3) to Eq. (A.1), Eq. (A.1) is developed as,

$$K_{\mathrm{u}} = \mathrm{g} \times \mathrm{cm}^{-1} \times \mathrm{s}^{-2}. \tag{A.4}$$

Joule (J) can be converted as,

$$\mathrm{J} = 10^{3}\mathrm{g} \times (100\ \mathrm{cm})^{2} \times \mathrm{s}^{-2}. \tag{A.5}$$

Hence, Eq. (A.4) is developed as,

$$K_{\mathrm{u}} = 10^{-1} \times \mathrm{J} \times \mathrm{m}^{-3}. \tag{A.6}$$

Therefore, K_{u} is in J/m^3.

APPENDIX B

In-plane magnetic anisotropy energy in Au/Co/Au thin film

Here in-plane magnetic anisotropy energy (K_u) in Au/Co/Au thin film is presented. Thin films were prepared on an ITO-coated glass substrate. The stacking of the thin films is ITO-coated glass sub. / Cr (5 nm) / Au (30 nm) / Co (6 nm) / Au (30 nm). The fabrication method is same to that of the Au/Co/Au nanostructure. Figure B-1 shows the L-MOKE (λ = 640 nm) and P-MOKE (λ = 750 nm) curves of the Au/Co/Au thin film. The saturated magnetic field of P-MOKE curve is about 110 times stronger than that of L-MOKE curves. This result indicates that (1) Au/Co/Au thin film has magnetic anisotropy and (2) the easy magnetization axis is parallel to the film plane.

K_u in the Au/Co/Au thin film was calculated using both L-MOKE and P-MOKE curves. The calculation method is same to that of the Au/Co/Au nanostructure in **Chapter 4**. K_u was calculated as 5.41×10^5 J / m^3. As described in **Chapter 4**, K_u is written as a sum of shape anisotropy energy (K_s) and magnetocrystalline anisotropy energy (K_i). In the case of a thin film, whose lateral dimensions are treated as infinitely long compared to its thickness, shape anisotropy leads to an in-plane magnetization in thin film. Therefore the sign of K_u and K_s is same. Usually, K_s in a thin film is described by $2\pi M_s^2$, where M_s is saturated magnetization in a magnetic thin film [B.1]. Moreover, K_i can be obtained by subtracting K_s from K_u. Table B.1 indicates K_u, K_s, and K_i in Au/Co/Au thin film. For calculating K_s in Au/Co/Au thin film, M_s = 900 emu / cm^3 in 6-nm-thick Co thin film was used [B.2]. From the table B.1, the sign of K_i is positive, which means that

magnetocrystalline anisotropy leads to in-plane magnetization in Au/Co/Au thin film.

Table B.1. K_u, K_s, and K_i in Au/Co/Au thin film.

K_u (10^5 J / m^3)	K_s (10^5 J / m^3)	K_i (10^5 J / m^3)
5.41	5.09	0.32

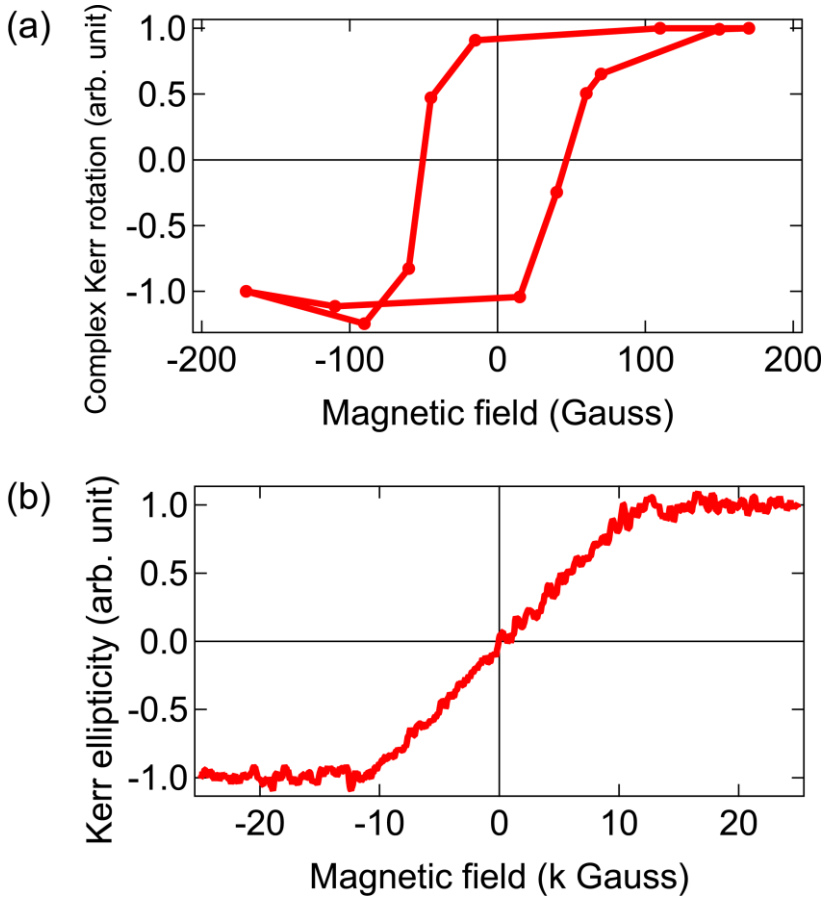

Figure B-1. (a) L-MOKE, and (b) P-MOKE curve for Au/Co/Au thin film.

References

B.1. T. Kojima, M. Mizuguchi, T. Koganezawa, K. Osaka, M. Kotsugi, and K. Takanashi, Japanese Journal of Applied Physics **51**, 010204-1 (2012).

B.2. T. C. Chuang, P. L. Su, P. H. Wu, and S. Y. Huang, Physical Review B **96**, 174406 (2017).